Topology Optimization of 3D Printed Flexural Elements

by

Aidan Bjelland

A Thesis Presented in Partial Fulfillment
of the Requirements for the Degree
Master of Science

Approved November 2020 by the
Graduate Supervisory Committee:

Narayanan Neithalath, Chair
Christian Hoover
Subramaniam Rajan

ARIZONA STATE UNIVERSITY

December 2020

ABSTRACT

Investigation into research literature was conducted in order to understand the impacts of traditional concrete construction and explore recent advancements in 3D printing technologies and methodologies. The research project focuses on the relationship between computer modeling, testing, and verification to reduce concrete usage in flexural elements. The project features small-scale and large-scale printing applications modelled by finite element analysis software and printed for laboratory testing. The laboratory testing included mortar cylinder testing, digital image correlation (DIC), and four point bending tests. Results demonstrated comparable performance between casted, printed solid, and printed optimized flexural elements. Results additionally mimicked finite element models regarding failure regions.

ACKNOWLEDGMENTS

While writing this thesis, I was able to receive a large deal of mentorship and gain considerable knowledge in the realm of topology optimization and concrete testing.

I first need to thank my committee chair Dr. Narayanan Neithalath, for his guidance through formulating the thesis problem, addressing my corners and questions throughout the project, and providing consistent and timely feedback on my work.

I would additionally like to thank my committee members Dr. Christian Hoover and Dr. Subramaniam Rajan for agreeing to serve on my committee and provide me feedback and guidance regarding my research.

Finally, I wish to thank my fellow graduate student Sooraj Nair for being an invaluable lab partner by providing feedback for my computer models, spending countless hours printing and testing with me, and assisting me with the data analysis for the project.

TABLE OF CONTENTS

Page

APPENDIX Page

LIST OF TABLES

Table Page

LIST OF FIGURES

Figure Page

Figure Page

CHAPTER 1

INTRODUCTION

Due to recent advances in 3D printing technology, mortar flexural elements can be manufactured without need of casting, opening the doorway to innovate design techniques. One such technique that is readily available for use in the design process of the 3D printed flexural elements is topology optimization.

Figure 1 outlines the main and sub objectives of the research project. Overall, the research project is founded on the relationship between computer modeling, testing, and verification.

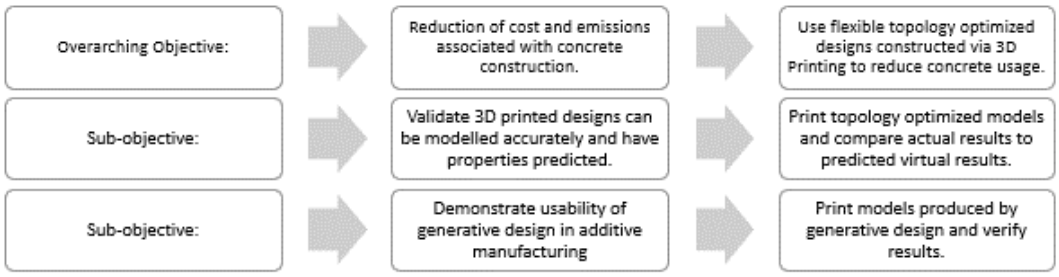

Figure 1. Objectives and sub-objectives of research project.

To achieve these objectives, computer modeling, small-scale printing, and large-scale printing were conducted. The small-scale testing served as a proof of concept behind material reduction and shape optimization. The results of these tests were considered in the 1st generation of computer models utilized for large-scale printing. Based upon the results of testing through digital image correlation (DIC) and four-point bending tests, a 2nd generation of computer models and prints were created and tested.

IMPACT OF TRADITIONAL CONCRETE CONSTRUCTION

One major concern about the concrete construction industry is the environmental impact of concrete production. A paper by Lowke, Dini, Perrot, Weger, Gehlen, and Dillenburger (2018) noted the following about the environmental impact of concrete:

> Considering the pronounced environmental impact of the construction industry (40% of global energy consumption, 38% of global greenhouse gas emissions, 12% of global potable water use, and 40% of solid waste generation in developed countries) and the carbon dioxide emissions due to the production of cement (5–7% of the global anthropogenic carbon emissions) saving material has not only a high economical but also high ecological impact (p. 50).

These points are further reiterated by Bos, Wolfs, Ahmed, and Salet (2016) who wrote:

> The production of cement is very energy intensive due to the burning of slag in a kiln. As a consequence, concrete production accounts for a significant per cent of the global CO_2 output (estimates and calculation methods vary, but the cement industry itself estimated that cement production is responsible for 5% of the global CO_2 output; World Business Council on Sustainable Development [WBCSD], 2002). The introduction of cement-replacers such as fly-ash (a blast furnace by product) has reduced the average concrete-related CO_2 output, but it is still significant. The fact that concrete raw materials are cheap, does not stimulate economical use and thus makes CO_2 reduction difficult (p. 209).

Furthermore, the impacts of concrete production extend outside environmental impacts.

Concrete casting requires immense amounts of labor which directly impacts the health and wellbeing of construction workers especially regarding the "erection of moulds and the placement of reinforcement" (Bos et al., 2016, p. 210). Potential health risks include: "eye, skin and respiratory tract irritation from exposure to cement dust; inadequate safety guards on equipment; inadequate lockout/tagout systems on machinery; overexertion and awkward postures; slips, trip and falls; and chemical burns from wet concrete" (Bos et al., 2016, p. 210).

3D PRINTING VS TRADITIONAL CASTING

3D printing offers many advantages to tradition casting as "[…] concrete elements with optimized shape can reduce the material needed, can become more compact, or reduce energy losses of buildings. Structural optimization and usage of additive manufacturing techniques can reduce the material input up to 70%" (Lowke et al., 2018, p. 50). The applications explored in Lowke et al (2018) also demonstrated that:

> A state-of-the-art report shows that these techniques are suitable for the direct production of small scale objects as well as construction elements using cementitious materials, geopolymers or sorel cement. The objects possess adequate strength, freedom of form and excellent contour precision (p. 64).

Another benefit of 3D printing is the ability to construct projects automatically as "[autonomous] or semi-autonomous 3D printers require minimal human surveillance" (Vantyghem, De Corte, Shakour, & Amir, 2020, p. 1). Vantyghem et al. also denotes an important aspect of 3D printing:

> Another outcome of the technique is that it disposes the need for conventional molding and allows for the creation of unique and complex shapes that were unattainable through conventional fabrication. By reducing the cost associated with nonstandard shapes, 3DCP gives virtual free rein to architects, designers and structural engineers enabling non-traditional design methods such as topology optimization (p. 1).

These newfound freedoms of design autonomy and automation of construction can revolutionize the design space and enable new avenues in construction.

These newfound freedoms are further commented on by Panda, Tay, Paul, and Tan (2018) who explain that "[the] potential of automation, elimination of formwork, reduction of construction waste, geometrical precision and production of complex geometries render 3D concrete printing an exciting prospect for the construction industry" (p. 672). These improvements to the construction industry are further padded by the fact that "[the] future of construction is most likely to be an integrated process that allows organizations to take advantage of both conventional and 3D printing technologies at the same time" (Panda et al., 2018, p. 672). As such, construction using 3D printing technologies is in a key position to best leverage the combined strength of conventional casting and 3D printing. De Schutter, Lesage, Mechtcherine, Nerella, Habert, and Agusti-Juan (2018) explained the long-term advantages of 3D printed concrete elements as follows:

> Implementing structural optimization as well as functional hybridization as design strategies allows the use of material only where is structurally or functionally

> needed. This design optimization increases shape complexity, but also reduces material use in [digitally manufactured concrete]. As a result, it is expected that for structures with the same functionality, [digitally manufactured concrete] will environmentally perform better over the entire service life in comparison with conventionally produced concrete structures (p. 34).

On the other hand, although a promising technology, 3D concrete printing is at the mercy of a wide array of parameters. For instance, "the properties of the hardened material are not only affected by concrete technological parameters like water/cement ratio or composition, granulometry and packing density of the dry mix, but also by the parameters of process technology" (Lowke et al, 2018, p. 64). The parameters associated with the 3D printing process are key in ensuring a high-quality print. These parameters include concrete age, mix temperature, mix internal pressure, density of printed material, and tool path (Bos et al., 2016, p. 217-221).

Concrete age is a key consideration in 3D printing, as 3D printing occurs over time. This means the age of the concrete is variable throughout the overall printing system and is a function of mixing and printing speeds (Bos et al., 2016, p. 221). Extruding the printed material may also cause issues depending on the mix. Low-slump concrete, which is necessary for free form printing, requires high pressures to be extruded (Bos et al., 2016, p. 221). However, this high-pressure extrusion can cause heating of the mix due to friction which can affect the properties of the mix (Bos et al., 2016, p. 221). As stated by Lowke et al., "The main challenge for future applications is the control of all the parameters linked processing in order to improve reliability and enable the prediction

of the mechanical behaviour of the printed elements" (2018, p 64). Future printing methodologies will need to successfully address these parameters for 3D printing to become commercially viable.

PRINTING OPTIMIZATION AND METHODOLOGIES

As 3D printing has many variables that affect the quality of the print, optimizing those parameters is of paramount concern. Tool path is one such area of printing optimization as tool path correlates to print quality. To prevent twisting of the filament being extruded by the nozzle, "printer head movement must be programmed such that the orientation of the nozzle always remains tangent to the tool path" (Bos et al., 2016, p. 212). Twisting of the filament prevents layers from laying horizontally, reducing uniformity and interaction between the layers (Bos et al., 2016, p. 212). If the tool path is optimally designed, the printer can avoid twisting, press layers against each other, and prevent gaps (Bos et al., 2016, p. 214-220). The pressing of layers is noted to "improve compaction as well as interface adhesion" (Bos et al., 2016, p. 220).

Another component of print optimization is creating the optimal printing apparatus. For a 3D printed concrete bridge designed and printed by Salet, Ahmed, Bos, and Laagland, the nozzle design was altered to ensure proper cable threading and interface bonding (2018, p. 227-229). For the project, the nozzle was changed from a down nozzle to a back-flow nozzle to a hybrid nozzle which illustrates the need to alter printing components for specific applications (Salet et al., 2018, p. 229).

Another vital factor in 3D printing is the interaction between print layers. Chandra, van Zijl Gideon, Tan, & Gibson stated "[interlayer] bond is integral to structural integrity and must be tested for appropriate design calculations" (2018, p. 796). To address issues with interlayer bonding, Hosseini, Zakertabrizi, Korayem, and Xu (2019) proposed a methodology to improve cohesion between layers by "adding a polymer consisting of sulfur and black carbon into interface of adjacent layers" (p. 118). Including the polymer increased "tensile cohesion between the two concrete segments [by] more than 100%" (Hosseini et al., 2019, p. 118). The technique was shown to be viable as the technique relied on "recycled, abundant and predominantly cheap materials (Hosseini et al., 2019, p. 118)." Similar chemical additives could be paramount in reducing the variability with the printing process.

3D printing also enables a wide array of printing methodologies. For instance, a method proposed by Borg Costanzi, Ahmed, Schipper, Bos, Knaack, & Wolfs demonstrated that segmented shell elements could be created "by printing and casting the object on an adaptable double curved surface, rather than a flat plane" (2018, p. 402). The paper demonstrates that the printing design apparatus is not limited to a nozzle but extends to the print bed itself (Borg et al., 2018).

3D printing methodologies can also be extended to arenas that traditional casting cannot. Mazhoud, Perrot, Picandet, Rangeard, & Courteille showed that 3D printing can extend to underwater projects (2019). Mazhoud et al. also mentioned the importance of optimizing print speed reiterating the importance of print speed in structural properties:

> Finally, for the underwater 3D printing materials, the compressive strength decreases with the increase of printing speed. In contrast to compressive strength, elastic modulus shows quite a different trend, below a critical printing speed the elastic modulus of 3D printable mortar decreases with increasing the printing speed (p. 466).

To extend 3D printing practices to "small construction activities such as window openings, electrical, mechanical, and finishing work or holes," Tay, Li, & Tan proposed methods for producing print support structures (2019, p. 269). Tay et al. concluded that "support structures [increase] both the manufacturing time and the post-processing operations" if not implemented properly (2019, p. 269). However, if implemented properly "support techniques can be combined to fabricate the main structure with the aim of reducing manpower, material waste and time required for production (Tay et al., 2019, p. 269)."

According to Chandra et al. "[reinforcement] is required to overcome quasi-brittle failure of concrete materials" (2018, p. 796). As such, several methods for reinforced 3D printing projects have been explored and tested. Chandra et al. suggested both manual and automatic approaches could be done to introduce reinforcement, given that more testing regarding anchorage and curtailment of the reinforcement would be done (2018). Another study by Asprone Auricchio, Menna, & Mercuri provides some credence to Chandra et al.'s claims. According to Asprone et al. "[the] initial flexural stiffness of the printed RC beam has resulted comparable with an equivalent full solid RC beam" (2018, p. 231). However, full parity was not achieved as "nonlinear flexural behaviour has been

influenced by local failure mechanisms, i.e. shear damage at the interfaces between adjacent concrete segments and steel-concrete anchoring failure" (Asprone et al, 2018, p. 231). Again, the influence of interlayer interfaces is shown to deeply impact the structural performance of printed elements.

Another method of reinforcement in the form of meshing was researched by Marchment and Sanjayan who inserted a "6 mm × 6 mm galvanised steel reinforcing mesh within single extruded layers" (2020, p. 10). Marchment and Sanjayan stated "[the] tests and calculations [indicated] the overlapped mesh was effective in working as a functional continuous reinforcement" and "increased moment strength in flexure by 170%–290%" (2020, p .10). The previously discussed reinforcement methods highlight that 3D printed elements is not limited to simple reinforcement techniques.

PRINTING MATERIALS

Due to the freedom afforded to 3D printing, new materials can be utilized for design elements. For instance, Xu, Zhang, Schlangen, Luković, & Šavija fabricated with "cementitious cellular composites (CCCs) with auxetic behavior" paving the way for application in "energy harvesting or vibration damping systems" due to the energy dissipation abilities of the material (Xu et al., 2020, p. 10).

Other researchers focused on producing materials which processed thixotropy which improves flowability during 3D printing. Panda, Singh, Unluer, & Tan developed a "3D printable one-part geopolymers that possess thixotropy property" and established how essential material fluidity and green strength were (2019, p. 617). Chen, Yang,

Zheng, Huang, Li, Zhao, Wang, Lu, & Cheng studied thixotropy through a calcium sulfoaluminate cement composite and determined that metakaolin could improve thixotropy and yield stress (2020). Zhang, Zhang, Liu, Yang, & Pang utilized a concrete ink with nano clay and silica fume to improve "thixotropy, green strength and buildability of this concrete" (2018, p. 270).

To reduce the need of formwork, Panda and Tan developed a "novel 3D printable geopolymer mortar […] which can be used for printing non-structural building components directly from digital models without the need of any formwork" (p. 10264, 2018). The geopolymer was based on fly ash (Panda & Tan, 2018).

As new materials are used in 3D printing, rheological models will need to be developed to improve material modeling for 3D printing. Jeong, Han, Choi, Lee, Yi, & Kim created one such model based on a Herschel-Buckley fluid (2019). Jeong et al. demonstrated the "proposed model would be very helpful to obtain the rheological properties of fresh concrete required for 3D printing, such as hardening coefficient and initial yield stress, without any complex numerical simulations" (p. 20).

TOPOLOGY OPTIMIZATION AND FINITE ELEMENT ANALSYS

3D printing requires optimized designs to be able to contend with traditional casting techniques. These designs are created using a processed called topology optimization which is based upon finite element analysis (FEA). The current state of topology optimization and FEA in additive manufacturing (AM) as put by Liu, Gaynor, Chen,, Kang, Suresh., Takezawa, Li, Kato, Tang, Wang, Cheng, Liang, and To (2018) is:

> Most of the existing algorithms can be better tuned or developed further – e.g., concurrently optimizing the build direction when performing overhang-free topology optimization. Additionally, many algorithms have not been closely linked to or validated by AM – e.g., the heterogeneous two-scale topology optimization algorithm and the robust topology optimization approaches, among others. Furthermore, increasingly more open problems emerge, such as the residual stress constrained topology optimization for metal AM. In addition, some problems are highly evaluated by industry but have not drawn enough attention from the research community – e.g., the expensive post-machining of the topological designs (p. 2476).

However, many promising formulations of topology optimization do exist.

Nana, Cuillière, and Francois "proposed an automatic process for reconstructing straight beam structures from topology optimization" (2017, p. 80). Nana et al. used an optimization approach "based on the SIMP method" which included a "curve skeletonization process" (2017, p. 80). The process proposed by Nana et al (2017) was as follows:

> Curve skeletons are approximated as straight beams with basic geometric circular cross sections. A mixed-dimensional beam-solid finite element analysis (FEA) is conducted to validate the optimized model topology and geometry. This mixed-dimensional FEA features minibeams elements to couple beam and 3D solid elements. With our approach, we are able to automatically reconstruct rough

> optimized results into CAD designs, which are then easier to modify, to manipulate, and to manufacture (p. 80).

Another approach by Longxuan, Wenfeng, Pengfei, and Mijia which was based on optimizing a three-branch joint demonstrated "the topology optimized joint [had] the best static behavior" and that "[high] precision joints can be produced by using 3D printing technology" (2020, p. 13).

Due to the flexibility of topology optimization and FEA, similar methodologies can be used for a variety of purposes. For example, Langelaar (2016) discussed the following method based upon density-based topology optimization:

> This paper presents a method to generate fully self-supporting, optimized part geometries in three dimensions. It combines established density-based topology optimization with a simplified AM process model, implemented as a layerwise nonlinear spatial filter defined on a uniform structured mesh. This formulation is able to rigorously exclude geometries from the design space that violate the overhang angle criteria typically encountered in AM processes. As a result, optimized designs do not require additional sacrificial structures to support overhangs, which simplifies post-processing and reduces cost (p. 69).

Safonov utilized a density-based topology optimization "to [find] the optimum configuration for local distribution of material density" for use in "three-dimensional continuous fiber-reinforced structures fabricated by composite additive manufacturing [processes]" (2019, p. 295). The algorithm developed "[produced] lighter structures [. . .]

with stiffness virtually equivalent to that of initial structures of anisotropic and quasi-isotropic materials" (Safonov, 2019, p. 296).

Ultimately, topology optimization and FEA can be utilized to address weaknesses of and offer new opportunities for additive manufacturing techniques. Podroužek, Marcon, Ninčević, & Wan-Wendner (2019) demonstrated the following with their paper on bio-inspired infill patterns:

> Based on the presented theoretical arguments and experiments it can be assumed that custom 3D infill patterns may be an interesting alternative to classical (2D) infills in additive manufacturing if (i) general stress states are likely to occur; or (ii) in case of complex geometries. 3D infills avoid introducing macroscopic anisotropy by additive manufacturing while still achieving large weight reductions (p. 499).

Podroužek et al. exhibited their "[lightweight] generative multi-scale design [could] […] potentially [offer] additional benefits in terms of tuned thermal, acoustic, static or dynamic properties" (p. 499). Xiong, Yao, Zhao, & Xie (2020) were able to address the issue of enclosed voids by offering a new topology optimization methodology:

> In this study, we have proposed a structural connectivity control approach based on the bi-directional evolutionary structural optimization technique. In this approach, the structural connectivity is evaluated during the optimization process. The shortest path is found to connect enclosed voids with the structural boundary. The enclosed voids are eliminated by generating tunnels along these paths. A

> hierarchical graph scheme is used to improve the computational efficiency of the approach (p. 10).

The results of the research showed the approach was “capable of creating structurally efficient designs without enclosed voids” and could “generate diverse and competitive designs by changing the radius and the number of tunnels” (Xiong et al., 2020, p. 10).

PRINTING APPLICATION

3D printing lends itself to many applications due to the flexibility in designs and materials used. Bos et al. stated that, “since the print head gradually builds up the complete structure, it is feasible that the composition and quantity of the printed material can be parametrically varied from one location to another, according to specific local requirements” (2016, p. 210). As such, a 3D printed structure could be composed of various components. The example exhibited by Bos et al. was a wall composed of an outer skin of self-cleaning concrete, an inner skin of acoustic concrete, a shell of high-performance concrete, and a core of insulating light weight concrete (2016, p. 210).

Further practical applications are discussed in Salet et al, by demonstrating the construction and use of a 3D printed concrete pedestrian bridge (2018). According to Salet et al. (2018):

> [. . .] the bridge was loaded with 10 containers filled with 500 litres of water. Including their self-weight, this resulted in a total load of 57 kN on the bridge. The containers were positioned in a pattern such that 100% of serviceability limit state bending moment was reached. The resulting deflections were too small to

> measure. As also no other response was observed, and in consideration of the previous material and scale testing, the bridge was considered to comply with the Dutch building regulations (p. 235).

The bridge was opened to the public after surface finishing was applied (Salet et al., 2018, p. 235). Overall, the project exhibited the applicability of 3D printing in actual application.

Another bridge was design by Vantyghem et al. that utilized a topology optimization to optimize a 2D rectangular domain of linear elastic concrete (2020, p.). The optimization procedure "[seeked] a design that [minimized] the displacements at the top surface of the beam, due to the combined action of the external loads and the post-tensioning tendon" (Vantyghem et al., 2020, p. 2). Once the 2D model had been optimized, the design was broken up into layers and components for printing (Vantyghem et al., 2020, p. 5). The overall manufacturing process was as follows (Vantyghem et al., 2020, p. 5-8):

1. Print girder elements.
2. Cast end blocks.
3. Assemble components.
4. Integrate reinforcement and grouting.
5. Post tension steel reinforcement.

The same procedure was mirrored by Salet et al. in their pedestrian bridge (2018, p 232-234). As large-scale printing applications cannot be constructed in one piece, assembly must be of paramount concern when designing printable structures.

CHAPTER 2

FINITE ELEMENT ANALYSIS AND TOPOLOGY OPTIMIZATION

Before a mortar beam can be printed, an STL model must be created. To create a model, the major phases of initial geometry, topology optimized model, and printable optimized model are followed. The steps included in each phase are outlined in Figure 2.

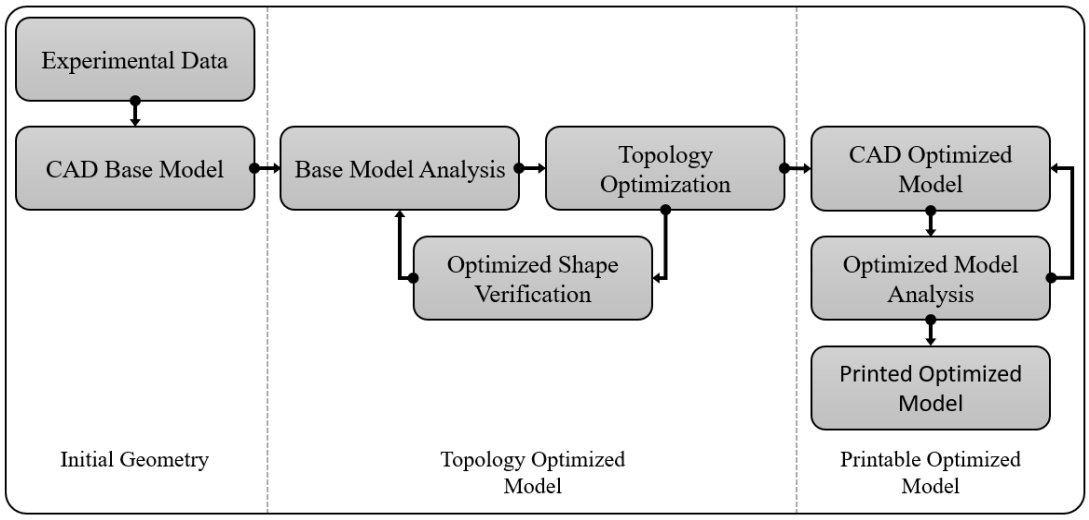

Figure 2. Workflow for completing a printable optimized model.

The first step is gathering material property data from experiments or online sources for the finite element analysis software. For mortar, these properties notably include compressive strength, Young's modulus, Poisson's ratio, and shear modulus. After inputting the necessary data for the analysis, a CAD base model must be constructed. Figure 3 (p. 17) displays a base model utilized for this project. The top face defines the edges and faces utilized to define four-point bending and uniformly distributed load cases respectively. The bottom face includes the edges where boundary conditions are applied. The figure also notes optimization exclusion regions where

topology optimization will not occur. The faces and edges on this geometry are based upon the testing configuration.

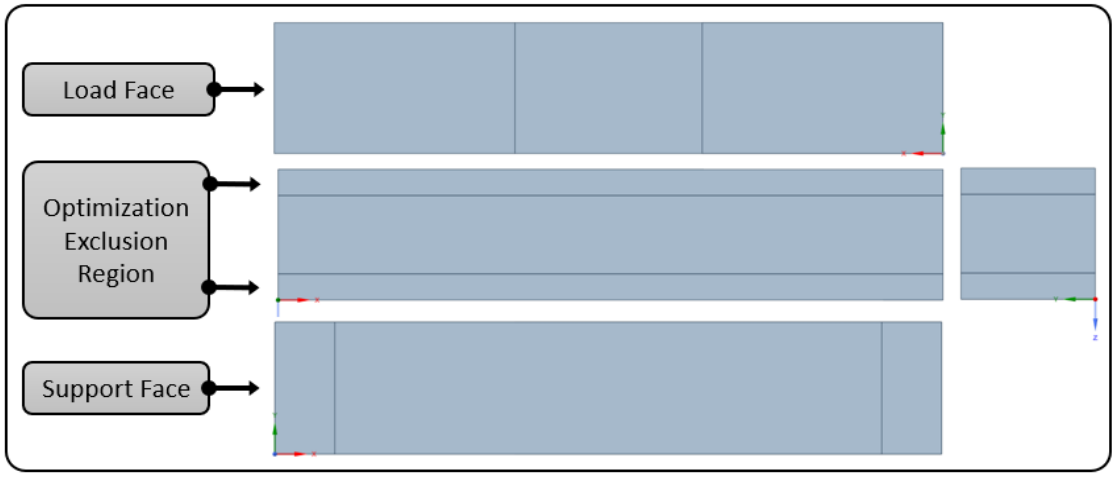

Figure 3. Base model geometry and regions.

After constructing a geometry, material properties and a mesh are defined. Next, loads and boundary conditions must be applied to respective edges and faces of the geometry. Once configured, the model can be analyzed, resulting in displacement and stress results.

Based on these results and specified constraints, topology optimization can be conducted. For the topology optimization conducted for this research, the constraints included the following: symmetry, extrusion, and global von-mises stress. Extrusion defines an axis in which the cross-sections will remain the same (ideal for printing). The objective utilized by the topology optimization software was to reduce mass as opposed to compliance. Compliance attempts to discover the configuration that will minimize the product of loads and displacements.

After the topology optimization is completed, the optimized model will be repaired and imported into another analysis model. The stress and displacement results are then compared to solid model to confirm parity. If the results are not consistent, the base model or topology optimization setting will need to be adjusted, and the optimization re-run. Figure 4 illustrates the typical result of a topology optimization.

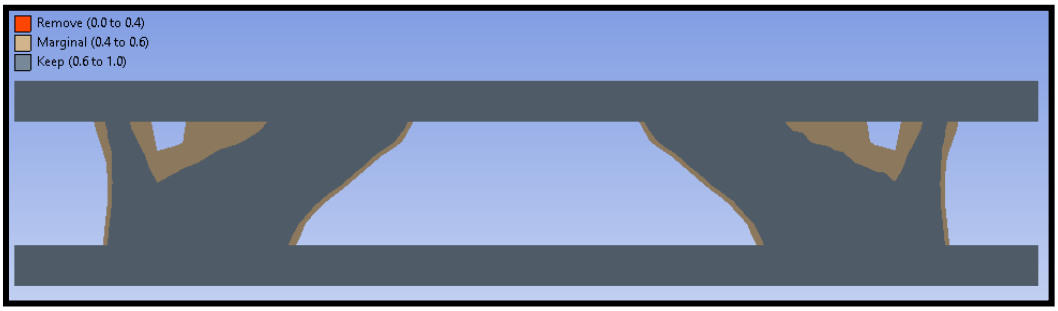

Figure 4. Results of optimizing solid model with four-point bending and uniformly distributed load.

The final component of model creation is adjusting the optimized shape to be printable, meaning that small holes must be removed and edges smoothed. The optimized printable model for Figure 4 is displayed in Figure 5.

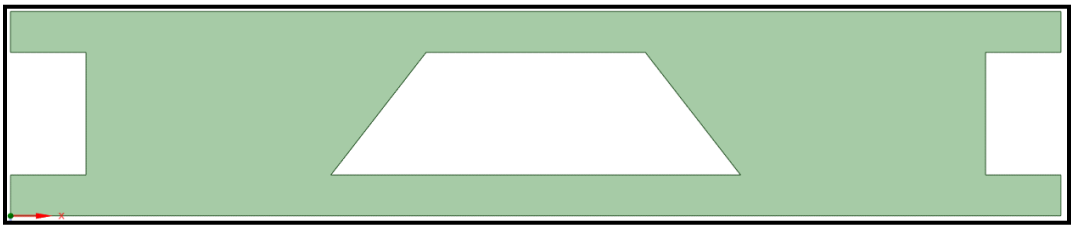

Figure 5. Results of removing small holes and smoothing edges for printability.

As a final check before sending the model off for printing is to analyze the model and confirm parity. If parity is not achieved, the steps conducted to achieve printability must be adjusted. An example of such a comparison for the minimum principal stress is shown in Figure 6.

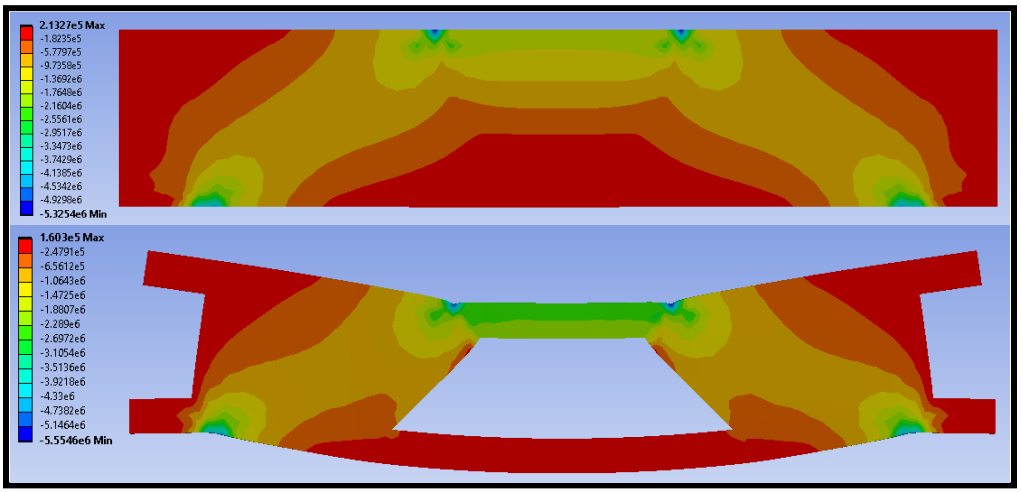

Figure 6. Comparison of minimum principal stress between solid and printable optimized models.

FIBER REINFORCED BEAM MODELING

Due to the constraints on how different bodies interact in finite element modeling, topology optimization for fiber and reinforced beams is limited. As such, fiber models were based upon modifications to the standard topology optimized design. For fibers, orientation is heavily influenced by print path. Thus, modelling the fibers required a region-based approach to generating the fiber distribution as displayed in Figure 7.

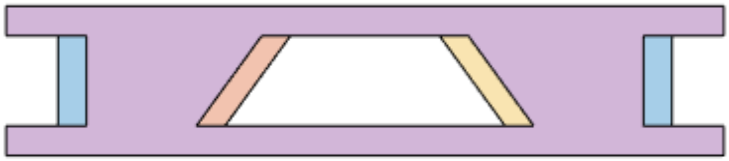

Figure 7. Regions defining principal orientation of fibers.

The fibers were modelled using line bodies created with a set of coordinates generated from a MATLAB program. The start node of these coordinate pairs was randomly distributed throughout the main body. Depending on what region, which is defined based upon print path, the orientation of the fiber is calculated within a range. Figure 8 (p. 21) shows a sample fiber distribution and orientation for the region in Figure 7.

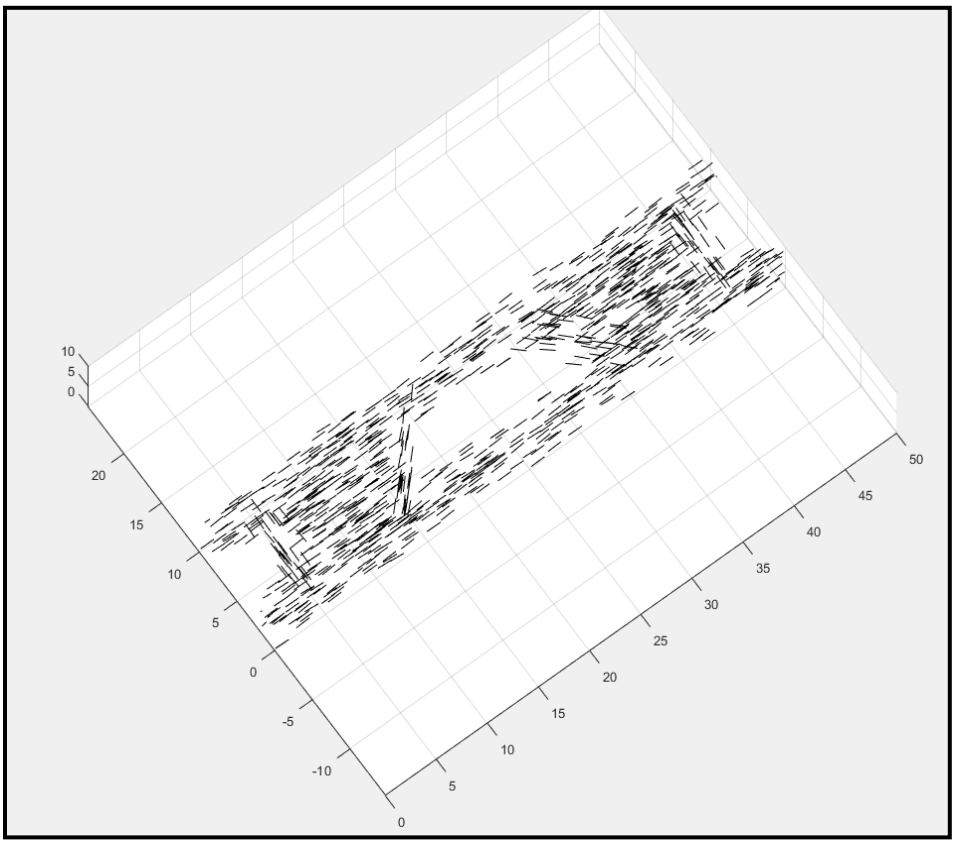

Figure 8. Sample distribution of fibers generated by the MATLAB program.

CHAPTER 3

SMALL SCALE PRINTING

To test the applicability of the 3D printing process and the concept of removing interior material to paste flexural beam elements, testing began by printing out small beams with 25%, 50%, 75%, and 100% infill percentages. The alignment of the infill in Slic3r, a G-Code creation software, was set to rectilinear. The flexural elements were composed of a mix that contained 30% limestone and 70% cement per 100 g of powder. The water-cement ratio was 41%.

The apparatus used to print these beams was a pastry printer which extruded the paste mix through a syringe onto the printing bed. Figure 9 illustrates a beam printed on the bed. For the printing apparatus, the bed controlled the x-y location of the nozzle. The z location of the syringe was controlled by a threaded vertical shaft connected to the arm containing the syringe.

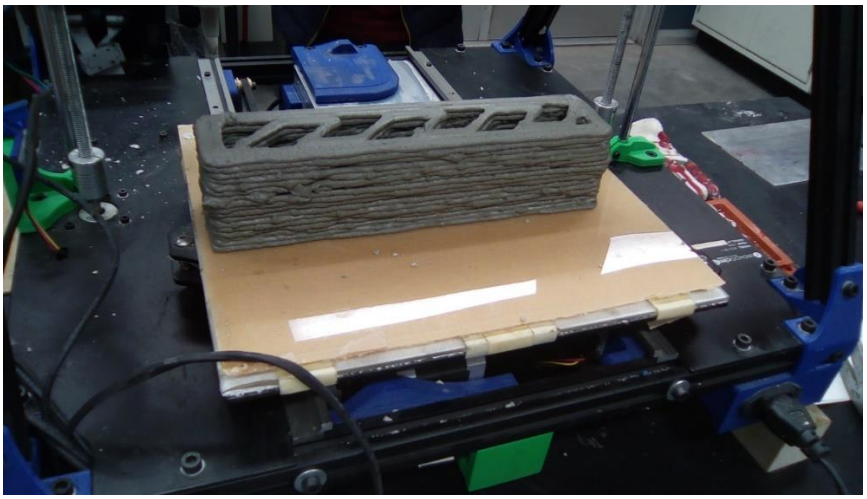

Figure 9. Print bed with printed beam.

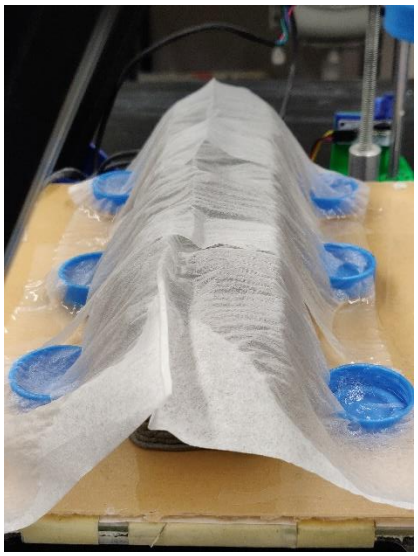

Figure 10. Wet paper towel applied after printing to prevent shrinkage cracking.

Before a printed beam can be moved to a curing chamber, the paste needs to harden. During the period required to harden the paste, shrinkage cracking is possible due to drying of the paste. To prevent any shrinkage cracking, a wet paper towel as shown in Figure 10 is utilized.

The 10 by 10 by 30 mm beams were tested after 14 days of curing under four-point bending. Figure 11 (p. 24) illustrates the testing apparatus utilized and the failure modes of the samples. Most of the failures appeared in the center span of the beams, indicating a failure due to bending. However, some beams appeared to fail under shear near the point of load application. The shear failure is believed to have been caused by a weak bonding between the interfaces caused by the print path. Weak interface bonding is often caused by paste not being extruded fast enough, which leaves small gaps between horizontal layers.

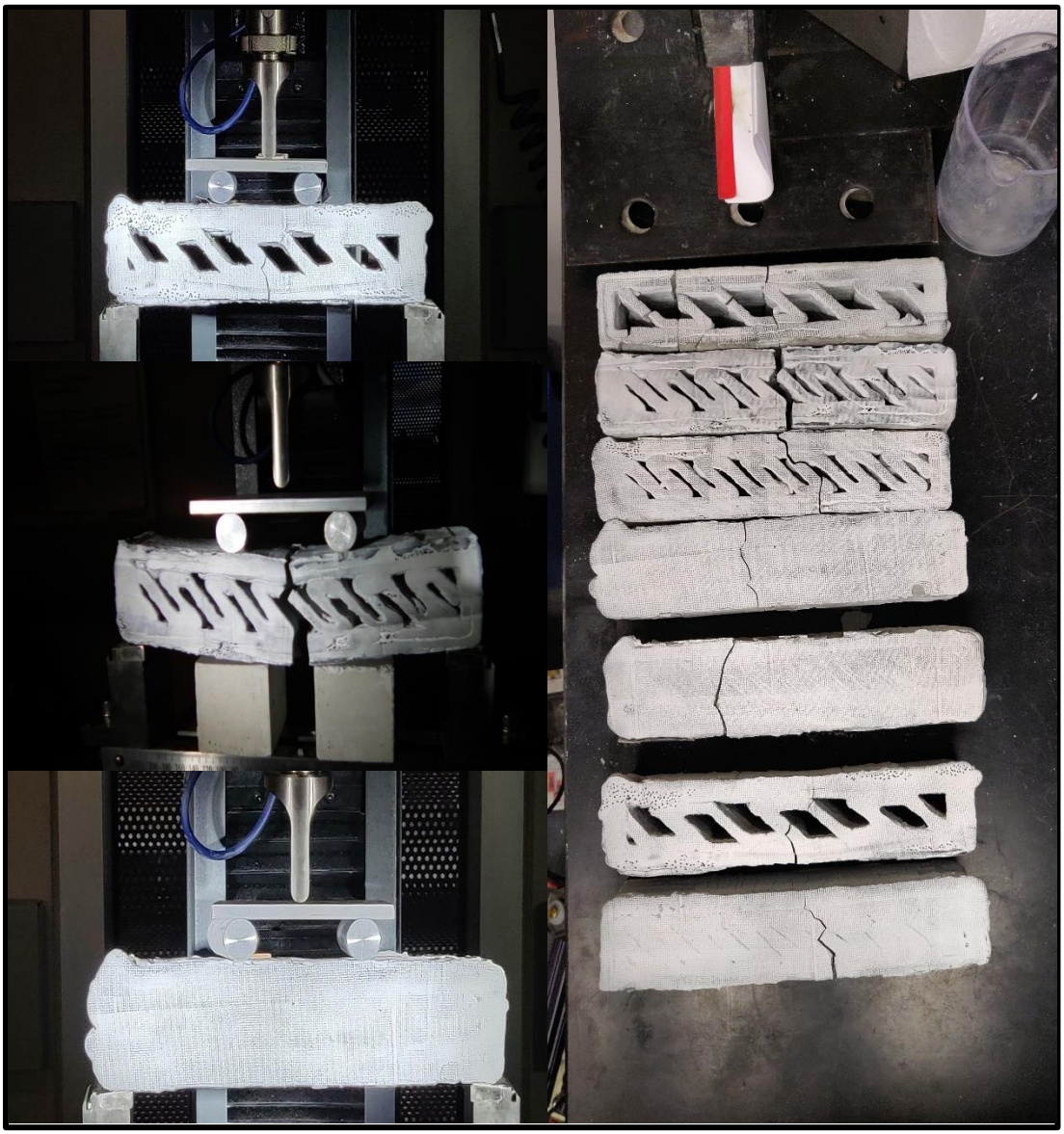

Figure 11. Pictures from testing (25%, 50%, and 100% infill) left and failure modes right.

Higher failure loads correlated with higher infill percentages with notable outliers as shown in Table 1. Overall, the percentage infill directly predicted the percentage of the maximum failure load. However, the variability with some outliers indicated design and print optimization could potentially lead to higher failure loads at lower infill percentages. On the other hand, poor printing practices could lead to less than desirable results, exhibited in the 75% infill case which only had 15.5% of the maximum failure load.

Table 1

Failure loads of specimens at various infill percentages.

Specimen: (Infill %)	**Failure Load: (N)**	**Percentage of Maximum Failure Load: (%)**
25%	615	22.9
25%	540	20.1
25%	1664	62.0
50%	1162	43.3
50%	1176	43.8
50%	1939	72.2
75%	415	15.5
75%	2351	87.5
100%	2686	100.0

MORTAR CYLINDER TESTING

Mortar cylinders, that had a diameter of four inches and height of eight inches, were also created and tested under compression during the small-scale printing. Following ASTM C469/C469M – 14, two test sets of cylinders were created to compute the value of Young's modulus and Poisson's ratio for a limestone sand mortar. The mix proportion for the mortar is listed in Table 2. These cylinders were tested at various fiber contents. For each fiber content, two cylinders were casted.

Table 2

Mix design utilized for mortar cylinders

Material:	**Percentage by Weight of Powder: (%)**
Cement	70
Limestone	30
Sand	89
Water	35
Super Plasticizer	0.25

The cylinders were tested using a SBEL Load Frame. First, the cylinders were encased by a compressometer to measure the horizontal and vertical strains of the specimen. An example of a tested cylinder with the compressometer loaded in the machine is displayed in Figure 12 (p. 27).

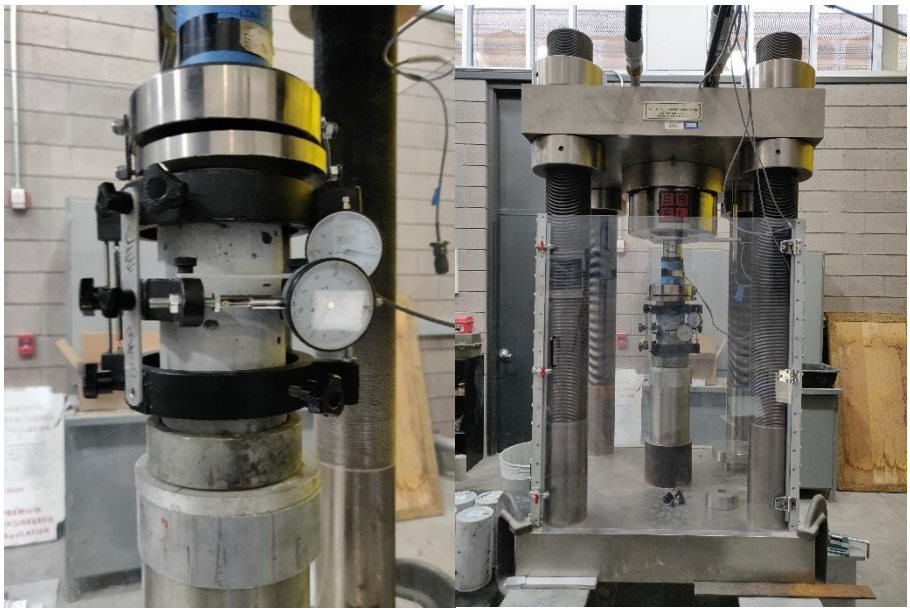

Figure 12. Concrete cylinder in testing apparatus with compressometer.

During the compression testing, the samples were seated with a load of 100 lbf before testing. The first phase of compression testing was in load control. After reaching a set load, the machine switched to displacement control for the duration of the test.

After compression testing, the Young's modulus and Poisson's ratio for both test sets were computed by taking the ratio of stress to vertical strain and ratio of vertical and horizontal strain respectively. Table 3 (p. 28) contains each specimen's Young's modulus and Poisson's ratio.

Table 3

Young's modulus and Poisson's ratio of mortar cylinders at various fiber contents

Specimen:	Set:	Fiber Content: (% Volume of Total Volume)	Young's Modulus: (GPa)	Poisson's Ratio:
1	1	0	15.45	~
2		0	14.41	0.25
3		0.32	14.57	0.25
4		0.32	16.43	0.25
5		0.54	13.79	0.11
6		0.54	16.5	0.29
7	2	0	14.70	0.15
8		0	14.86	0.20
9		0.32	15.64	0.23
10		0.32	17.28	0.19
11		0.54	18.76	0.28
12		0.54	18.21	0.25

The results of the tests illustrated that Young's modulus gradually increased with fiber content and that poison's ratio on average stayed the same at around 0.25 on average.

Due to testing limitations, the previous tests' compressive strengths extended beyond the maximum load of the machine, smaller concrete cylinders (3" by 6") were created and tested. These samples also followed the same mix design and were tested at 14 days. The Young's modulus and compressive strength for these samples is listed in Table 4 (p. 29).

Table 4

Young's modulus and compressive strength of mortar cylinders at various fiber contents

Specimen:	**Fiber Content: (% Volume of Total Volume)**	**Young's Modulus: (ksi)**	**Strength: (psi)**	**28 Day Projected Strength: (psi)**
F – 1	0	960	7888	9400
F – 2	0	1119	8975	
F – 3	0.32	964	7769	9208
F – 4	0.32	1025	8806	
F – 5	0.54	1190	9319	10048
F – 6	0.54	1087	8769	

The Young's modulus and compressive strength from these test results were utilized as estimates for the finite element model used for the large-scale designs.

CHAPTER 4

LARGE SCALE PRINTING

Large scale printing included the design, printing, testing, and verification of two generations of topology optimized flexural beam elements. The 1st generation was based primarily on a basic understanding of topology optimization and small-scale printing. The 2nd generation built upon the success and failures of the 1st generation of designs.

1st GENERATION

The first generation of designs were created using the geometry displayed in Figure 13 (p. 31). In the top image, the grey region denotes the to-be-optimized region of the design. The blueish-grey region was excluded from optimization. For this generation, the geometry was set to represent a four-point bending case. Along the A and B line, a load of 500 N was placed for a combined load of 1000 N. A fixed support condition was applied along the C and D face.

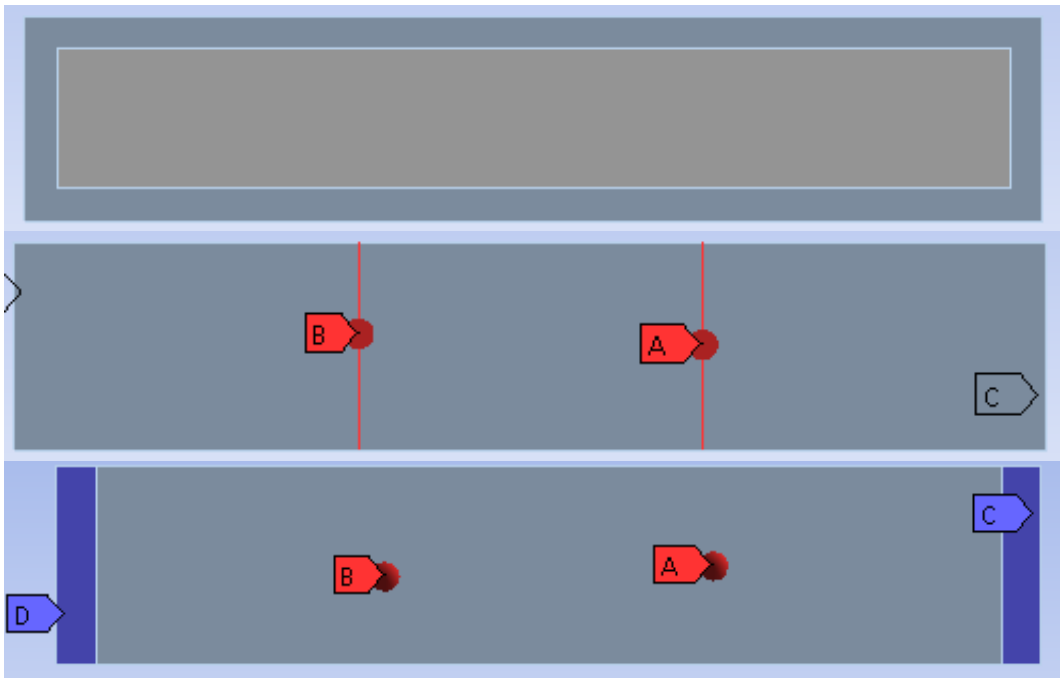

Figure 13. Side, top, and bottom views of base geometry used in 1st generation.

The objective utilized for the topology optimization was compliance. As previously discussed, this leads to a design that minimizes the product of load and displacement. Normally, this would lead to a solid section. However, a response constraint which required the mass to be reduced to 30% was applied. To ensure the design was printable, two manufacturing constraints were applied: symmetry and extrusion. The symmetry ensured both halves of the design were mirrored. Additionally, extrusion ensured the out of plane sections of the model remain consistent. The result of the topology optimization is displayed in Figure 14 (p. 32).

Figure 14. Optimized model for 1st generation of beams.

When the optimized model is compared to von Mises equivalent stress, maximum principal stress, and minimum principal stress, the reason behind the location of the remaining mass becomes clear. The location of the inner webs corresponds to the locations of greatest stress in Figure 15.

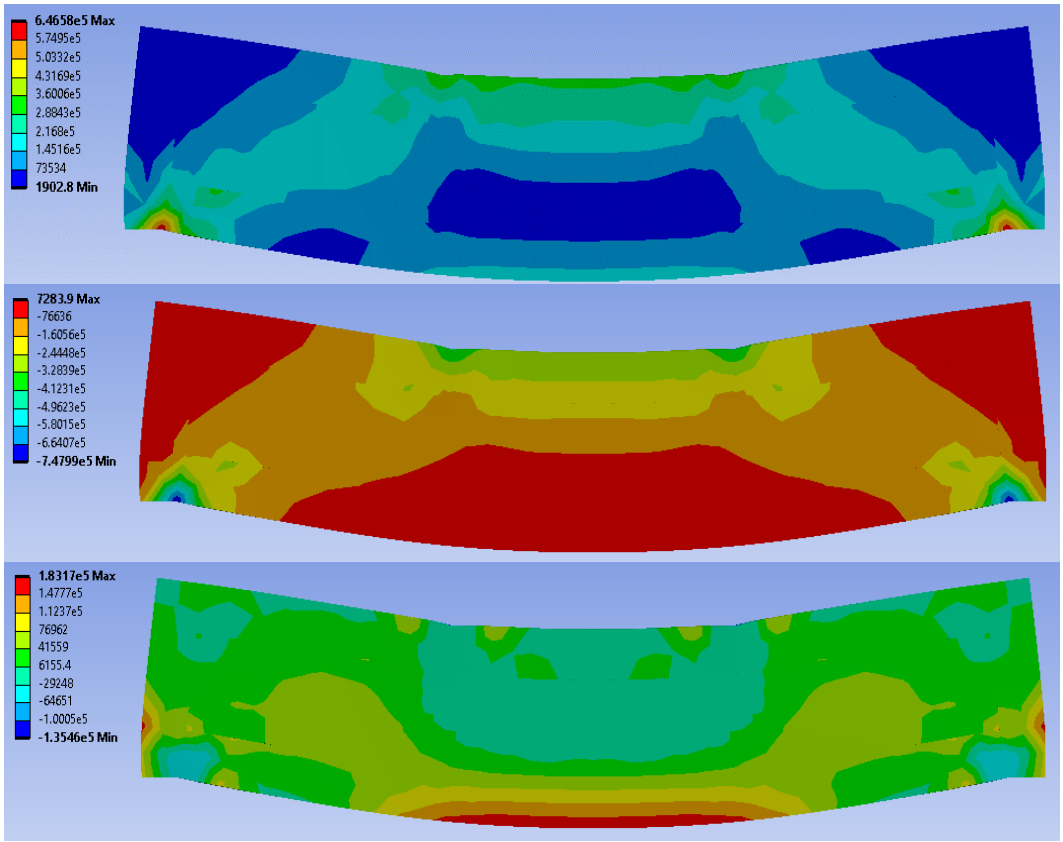

Figure 15. 1st generation solid geometry's von Mises, maximum principal stress, and minimum principal stress distributions (Pa).

To print the first generation of beams, a mix needed to be created. The mix design for the mortar beams consisted of cement, limestone, sand, and water. The quantity and proportion of these materials is listed in Table 5.

Table 5

Mix design utilized for 1st generation of beams

Material:	**Amount: (kg)**	**Percentage by Weight of Powder: (%)**	**Percentage by Weight Total Mix: (%)**
Cement	29.69	70.0	31.3
Limestone	12.73	30.0	13.4
Sand	37.61	88.7	39.6
Water	14.85	35.0	15.6
Super Plasticizer	0.12	0.28	0.1
Total	95	~	~

The 1st generation of beams included three casted, one solid printed, and four optimized printed beams. The failure loads for each beam are displayed in Table 6. Overall, the results of the testing were inconclusive, as three of the optimized beams were completely untestable.

Table 6

Failure loads for specimens in 1st generation.

Specimen:	**Failure Load: (N)**	**Failure Load (AVG): (N)**
Cast - 1	6023	5083
Cast - 2	4092	
Cast - 3	5133	
P_{solid} - 1	7246	~
P_{opt} - 1	2682	~
P_{opt} - 2	~	
P_{opt} - 3	~	
P_{opt} - 4	~	

The reason for the failure of the optimized beams was because the 1st generation suffered from four issues due to the printing process and design:

- Weak binding due to segmented printing path and sharp pathing angles.
- Shrinkage cracking due to slow printing and insufficient superplasticizer usage.
- Material waste due to unnecessary outer perimeter.
- Testing machinery configuration did not match configuration used in topology optimization.

These issues can be seen by examining Figure 16, with the most obvious error being the gaps along the bottom fiber. Figure 16 also displays the printing apparatus which is a down nozzle being fed via a hopper with an auger.

Figure 16. 1st generation optimized beam throughout the printing process.

Figure 17. Failure modes of printed and casted beams in 1st generation.

For the 1st generation beams, the failure modes are demonstrated in Figure 17. The casted and solid print beams failed in the center, indicating failure due to bending. One of the printed optimized beams failed in the center region as well, exhibiting the same failure due to bending. However, the second optimized beam that was able to be tested failed instantly in shear failure along a print path interface.

Figure 18 displays a snapshot taken from DIC for the first casted beam. The strain concentrations indicated where the crack was propagated. The results were consistent with typical understandings of bending failure in the tension region of a flexural mortar element. Figure 19, which is the solid printed beam, also displayed the same expected behavior.

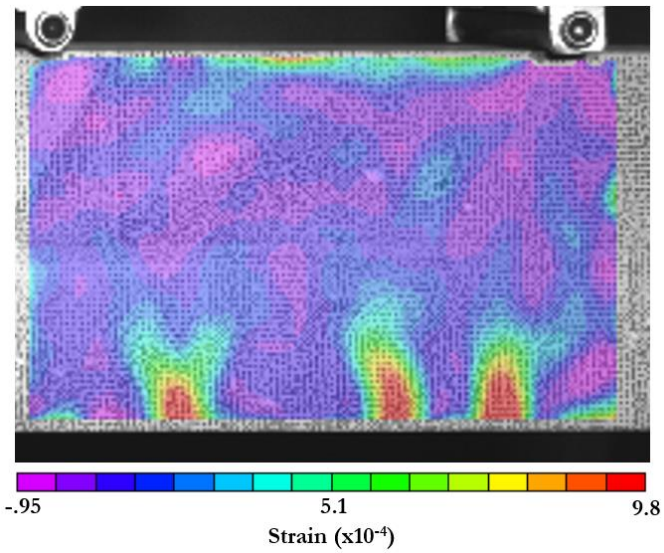

Figure 18. DIC of 1st casted beam in 1st generation.

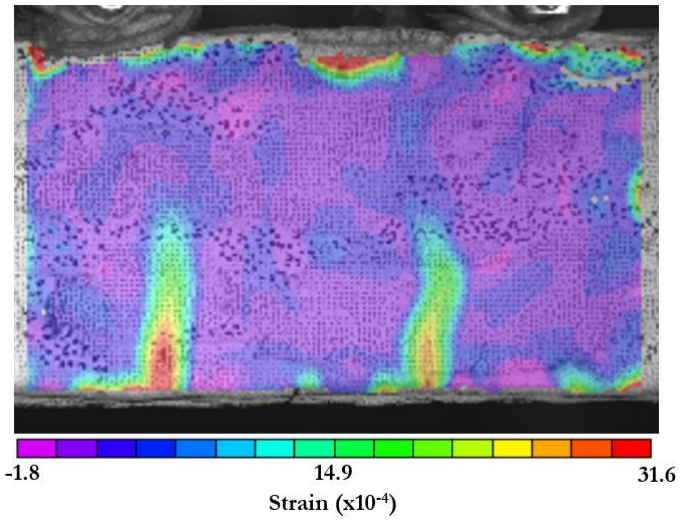

Figure 19. DIC of printed solid beam in 1st generation.

For the optimized beam, behavior was more closely dictated by the quality of the print. For the first optimized beam in Figure 20, no obvious location of crack propagation was present outside some strain concentration along the flanges. In Figure 21, a large strain concentration is located on the left along an existing crack produced during printing. The crack caused the instant shear failure of the second optimized beam.

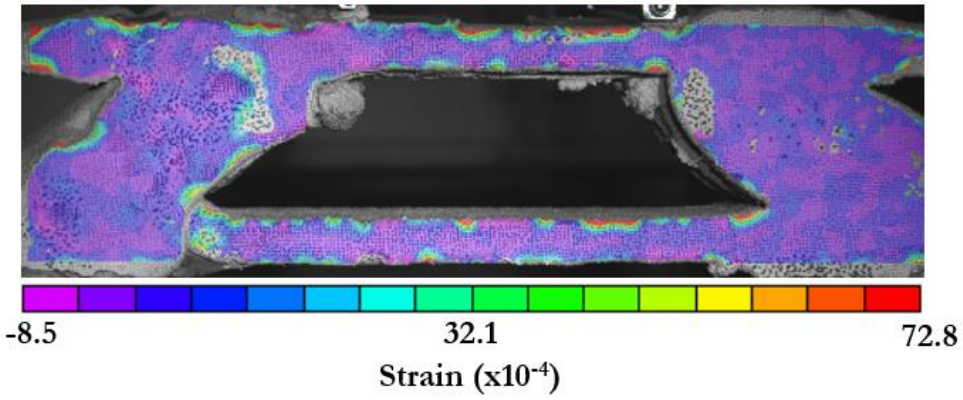

Figure 20. DIC of 1st optimized printed beam in 1st generation.

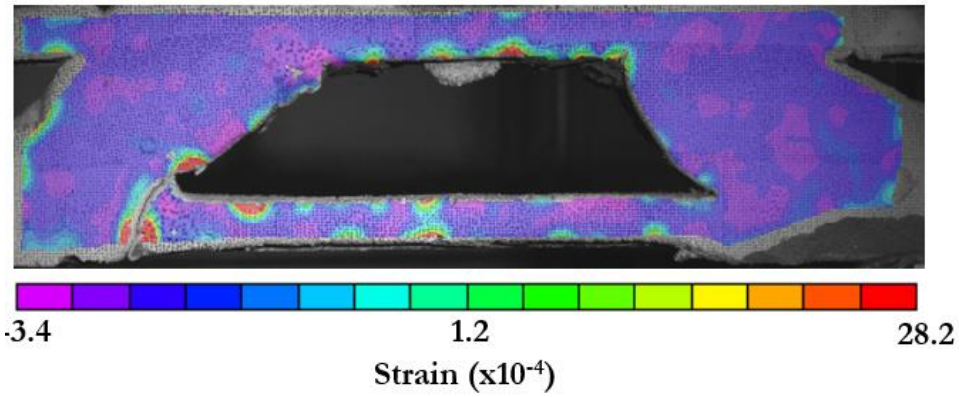

Figure 21. DIC of 2nd optimized printed beam in 1st generation.

2nd GENERATION

To address the failings of the 1st generation, the 2nd generation needed to see improvements to the modeling and printing process. The 2nd generation designs were optimized in respect to a 6000 N four point bending load case and 6000 N a uniformly distributed load case as displayed in Figure 22.

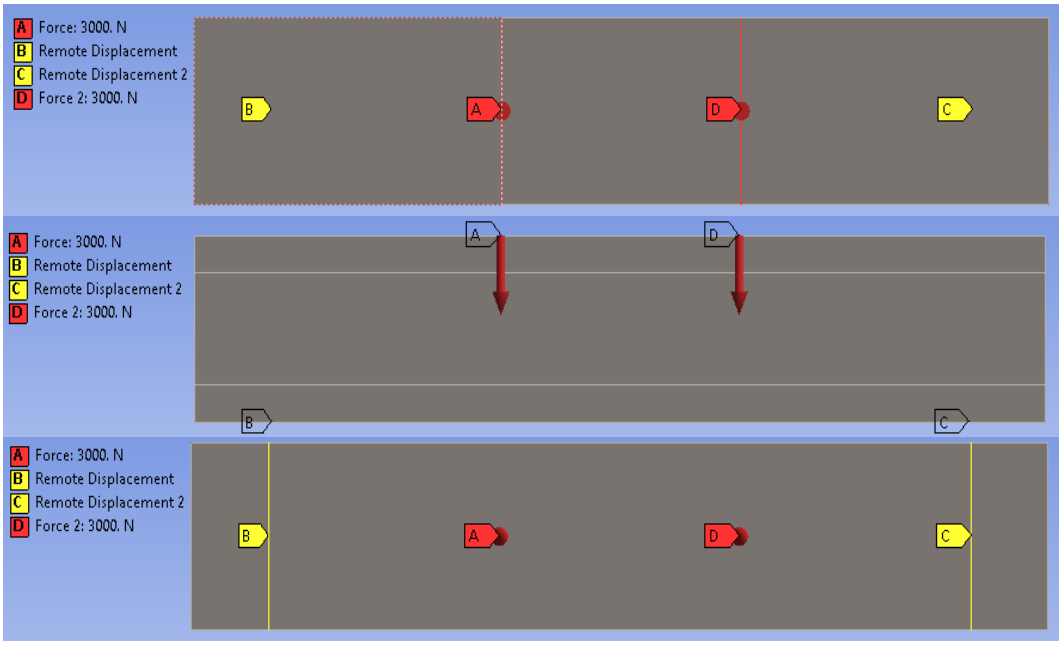

Figure 22. Top, side, and bottom views of base geometry used in 2nd generation.

Unlike the 1st generation which used fixed supports to model the support conditions, the 2nd generation used remote displacements. Remote displacements prevent stress singularities and better model a four-point bending geometry by guiding the displacements and rotations about a remote point. In this case, the remote points were placed below the midpoint of B and C. These remote points had the properties of no displacement and no rotations except in the out of plane direction. The distances where

the loads and supports were placed correspond to the exact locations on the testing apparatus. Using the exact measurements ensured a fair comparison between the computer model and the printed beams.

Additional improvements to the model arose out of reducing the excluded optimized perimeter to the top and bottom regions only. The reason for these regions being excluded from optimization was to allow the design to have the potential of being tested under various loading conditions and so that tensile reinforcement could be added.

Regarding topology optimization, all objectives and constrains were re-evaluated. As previously discussed in the second section of this report, the objective was switched to minimize mass. The response constraint was switched to be based upon the von Mises stress criterion of 1.75 MPa instead of a restrictive mass criterion. The change in response criteria enabled the optimized geometry to better model the stress concentrations in the solid geometry. The previously mentioned manufacturing constraints of symmetry and extrusion remained unchanged.

The equivalent von Mises stress distributions of the solid geometry, optimized geometry, and print geometry shown in Figure 23 (p. 40) are quite similar in shape and magnitude. The distributions demonstrate how closely the topology optimization adheres to the stress distribution of the solid geometry.

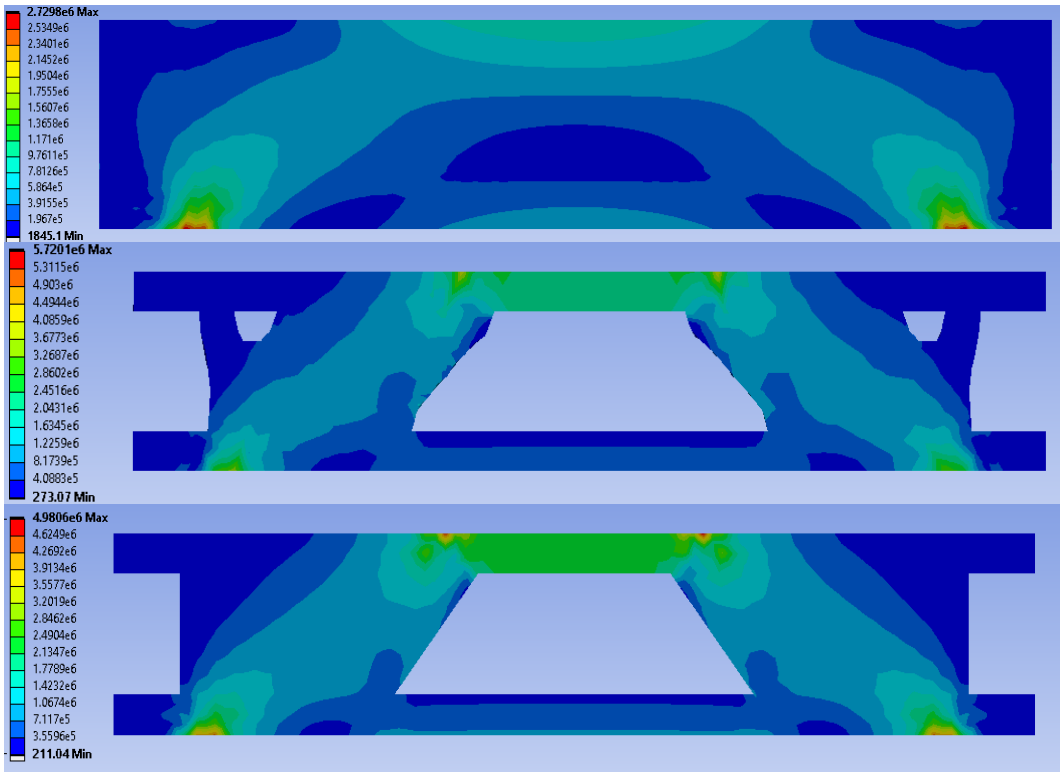

Figure 23. 2nd generations von Mises stress distribution (Pa) for solid, topology optimized, and print geometries.

The mix proportion between generations did not change except for the amount of super plasticizer utilized. The 2nd generation used 0.35% by weight of powder versus 0.28% used by the 1st generation. Table 7 (p. 41) displays the mix design used for the 2nd generation of beams.

Table 7

Mix design utilized for 2nd generation of beams

Material:	**Amount: (kg)**	**Percentage by Weight of Powder: (%)**	**Percentage by Weight Total Mix: (%)**
Cement	30.3	70.0	31.3
Limestone	12.98	30.0	13.4
Sand	38.37	88.7	39.6
Water	15.15	35.0	15.6
Super Plasticizer	0.15	0.35	0.1
Total	96.95	~	~

To improve the printing process, the 2nd generation saw increased print speed and a pre-extrusion amount applied at discontinuities in the G-code. Due to faster printing, drying in the mix was less of a factor during the print. A wetter mix combined with gaps being filled at discontinuities, lead to less gaps in the overall geometry. Figure 24 (p. 42) when compared to Figure 16 (p. 34) shows the clear improvement between generations.

Before testing, the load and support faces of the printed beams were cut using a saw. By smoothing these faces, the printed beams were able to sit properly on the supports and load concentration due to partial contact were prevented. White spray paint and black dots were applied after cutting for DIC purposes. For the four-point bending test, a load control of 100 lbf/min was done until a set load and then displacement control of 0.1 mm/min was done until failure.

Figure 24. 2nd generation optimized beam throughout the printing process.

Table 8 (p. 43) catalogs the failure load in newtons and Young's modulus for each specimen in the 2nd generation. The measured Young's moduli were not accurate due to the displacements measured by the machinery not being able to isolate the displacement of just the specimen. Based on the DIC conducted in tandem with the machinery, the actual displacements were on average 65% of the measured displacements. As such, a correction factor of 1.54 (1/0.65) was applied to the Young's moduli. The measured data and regions used for the measured Young's modulus can be found in the Appendix.

The printed beams offered loads far greater than the design load of 6000 N and the printed solid were outperformed by the optimized counterparts. Sadly, the casted beams underperformed due to unknown reasons preventing an accurate comparison between them and the printed beams. Due to the consistency between failure loads and Young's moduli of the printed beams, the optimized beams appear to have achieved the objective of reducing material used (26.5% volume reduction) while maintaining a comparable load capacity to the solid print.

Table 8

Failure loads and Young's modulus for specimens in 2nd generation.

Specimen:	**Failure Load: (N)**	**Failure Load (AVG): (N)**	**Measured Young's Modulus: (GPa)**	**Corrected Young's Modulus: (GPa)**
Cast - 1	4639	4405	0.72	1.1
Cast - 2	4780		0.79	1.2
Cast - 3	3796		0.64	1.0
P_{solid} - 1	7238	~	1.02	1.6
P_{opt} - 1	8641	9538	0.83	1.3
P_{opt} - 2	10670		0.71	1.1
P_{opt} - 3	9460		0.84	1.3
P_{opt} - 4	9380		0.90	1.4

The failure of the optimized beams appears to have been shear, with the cracks propagating to the left and right of the center hole. The angle of these cracks varied from about 16 to 30 degrees illustrated in Figure 25. The region of failure coincides with a region of high stress in the computer models as displayed in Figure 23 (p. 40). An alternative explanation is that this region coincided to a change in print path, hinting that a lackluster bonding of the horizontal interfaces could have caused the shear failure. There is some obvious evidence of cracking along an interface in the 3rd optimized beam. The solid casted and printed beams all failed in the center portion in the beam which is consistent with a general understanding of concrete failure in flexure.

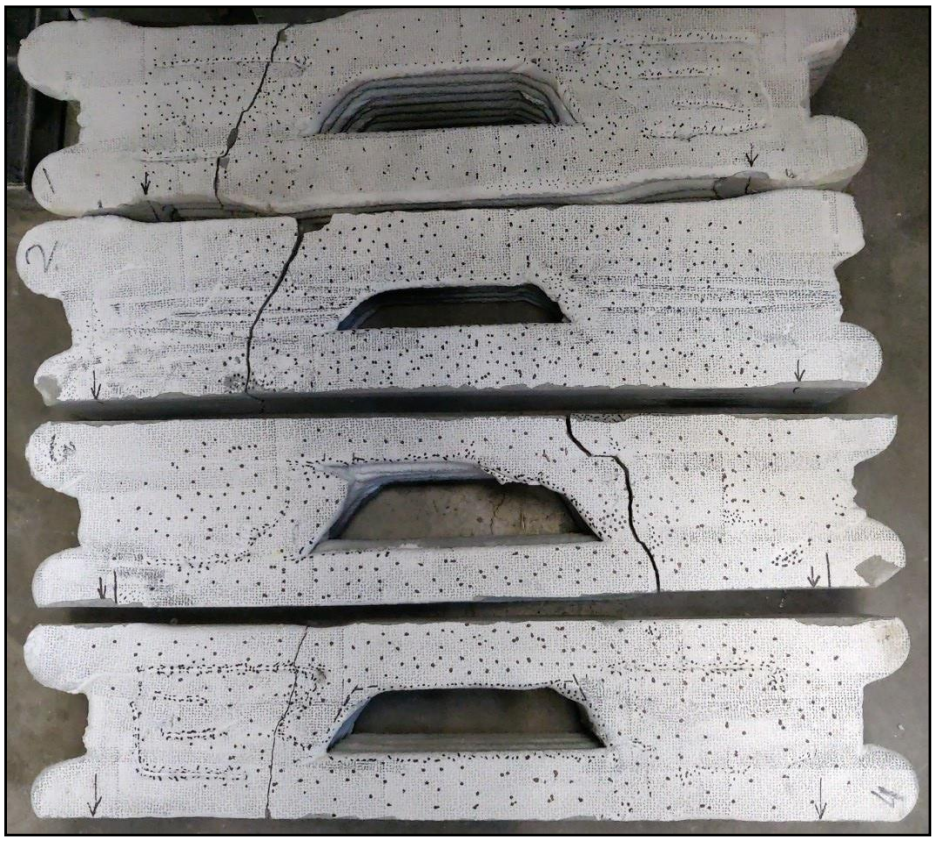

Figure 25. Failure modes of printed and casted beams in 2nd generation.

The hypothesis behind shear failure is further supported by the DIC when compared to the original print path followed by the design which is displayed in Figure 26. Here the interface between print paths can be clearly seen. When the DIC in Figure 27 and 28 (p. 46) are examined for the optimized beams, the crack is propagating along the interface.

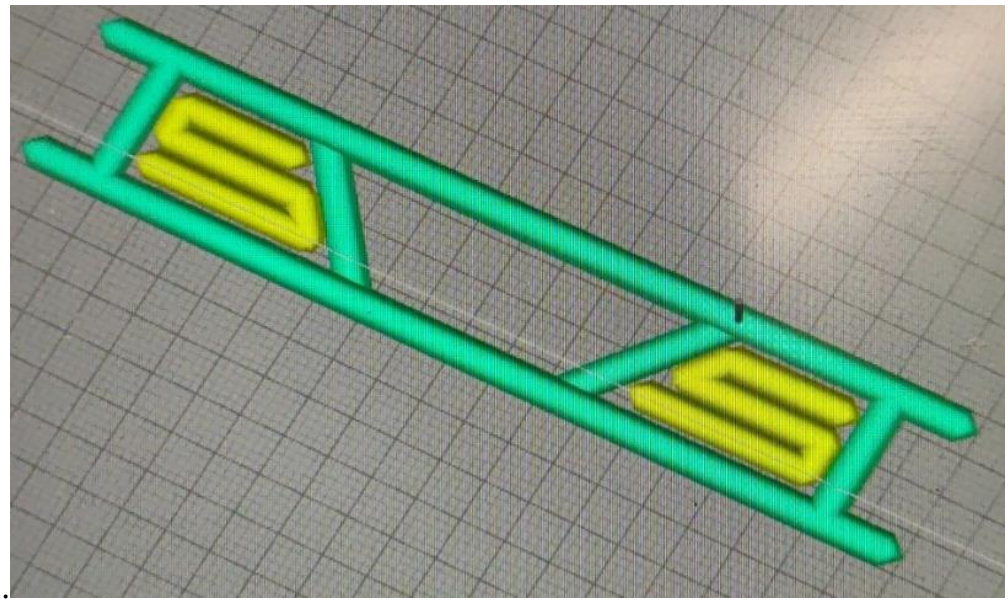

Figure 26. Print path for 2nd generation of optimized beams.

Figure 27. DIC of 1st optimized printed beam in 1st generation.

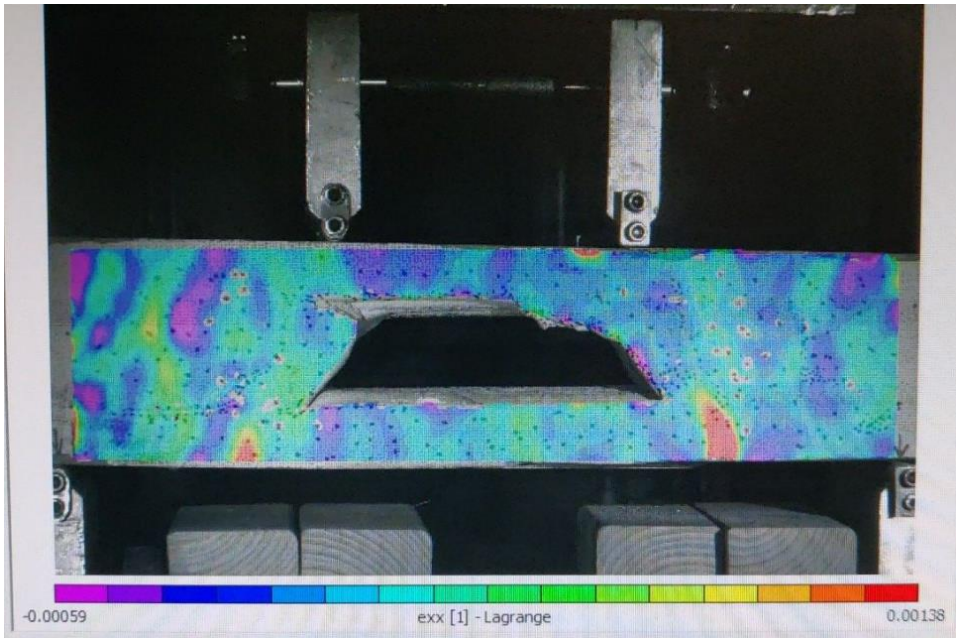

Figure 28. DIC of 3rd optimized printed beam in 2nd generation.

2nd GENERATION FIBER

To further explore the validity of the optimized geometry and to test the feasibility of adding fiber to a 3D printed beam, a second set of 2nd generation beams were created. The fibers used were brass coated steel fibers that were 13 mm long and 0.2 mm in diameter. The weight of fibers used in the mix was determined by calculating the amount of fibers needed to fill 1% of the volume of the powder mix. The mix proportions for the beam are in Table 9.

Table 9

Mix design utilized for 2nd generation of fiber beams

Material:	**Amount: (kg)**	**Percentage by Weight of Powder: (%)**	**Percentage by Weight Total Mix: (%)**
Cement	30.2	70.0	30.9
Limestone	12.94	30.0	13.2
Sand	38.25	88.7	39.1
Fiber	1.13	2.6	1.2
Water	15.1	35.0	15.4
Super Plasticizer	0.151	0.35	0.2
Total	97.77	~	~

The apparatus used to test the beams under four-point bending is displayed in Figure 29 (p. 48). Like in the non-fiber case, the fiber beams were cut beforehand for proper sitting and painted for DIC.

Figure 29. Apparatus utilized to test fiber beams under four-point bending.

For all beams, the first phase of the four-point bending test was in load control, with the load of 500 lbf/min being applied. At 1500 lbf, the samples switched to displacement control. The rates for displacement control were as follows:

- 1 mm/min for the first casted and solid print beams.
- 0.5 mm/min for the second casted and solid print beams.
- 0.1 mm/min for the optimized beams.

The displacement rates were higher at the beginning due to fibers extending the length of the test due to post-peak behavior. The rates were reduced later to attempt to smooth out the transition to post-peak behavior.

Table 10 lists the failure loads for each type of beam after 14 days of curing. The reason why the first optimized fiber beam is separated in terms of results is due to a change in print path. This print path altered to bottom and top flanges to be about two centimeters larger in the second and third optimized fiber beam.

Table 10

Failure loads for specimens with fiber in 2nd generation.

Specimen:	**Failure Load: (N)**	**Failure Load (AVG): (N)**
Cast - 1	10613	10010
Cast - 2	9407	
P_{solid} - 1	7077	7931
P_{solid} - 2	8785	
P_{opt} - 1	6151	~
P_{opt} - 2	9248	9366
P_{opt} - 3	9484	

The failure loads demonstrate that the optimized beams go toe to toe with the casted and solid printed beams. Furthermore, the reduced geometries show that major reductions in material usage can be done without major losses in failure loading. Figure 25 (p. 50), which displays the failure mode, shows that the optimized beams failed under bending. Since the optimized fiber beams failed under bending and the non-fiber beams failed under shear, the fibers appear to have reinforced the bonding at the horizontal interfaces. These results indicated that shear failure along the stress concentrations correlates with weak interface bonding.

Figure 30. Failure modes of printed and casted fiber beams in 2nd generation.

Another important aspect of the fiber beams was that of post-peak behavior. All the fiber beams tested exhibited bridging across any formed cracks and the fiber bridging prevented instant collapse of the beams. For the optimized beams, the crack fully propagated through the bottom flange and a new crack began forming on the top flange. The crack propagation before and after partial failure can be examined in Figure 31 and 32 (p. 51).

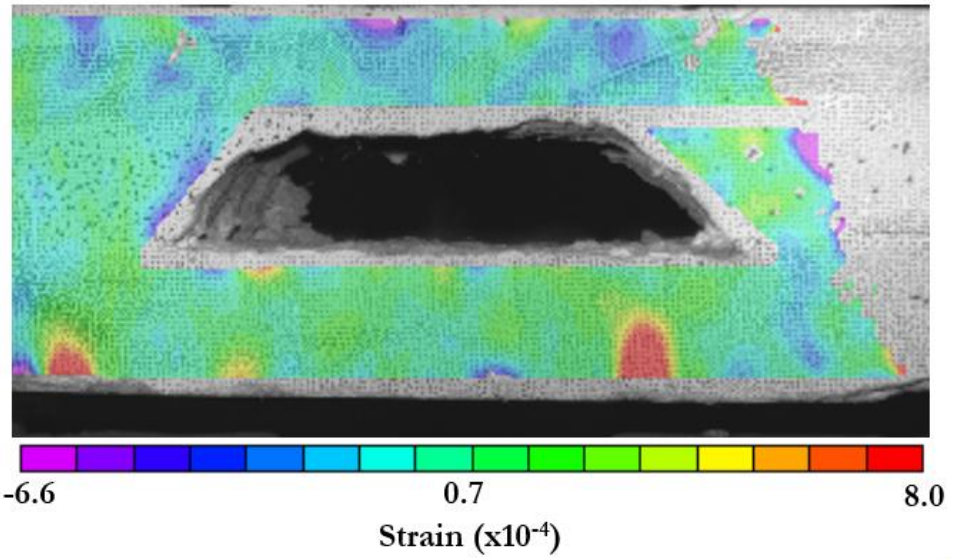

Figure 31. DIC of 2nd optimized fiber printed beam in 2nd generation before failure.

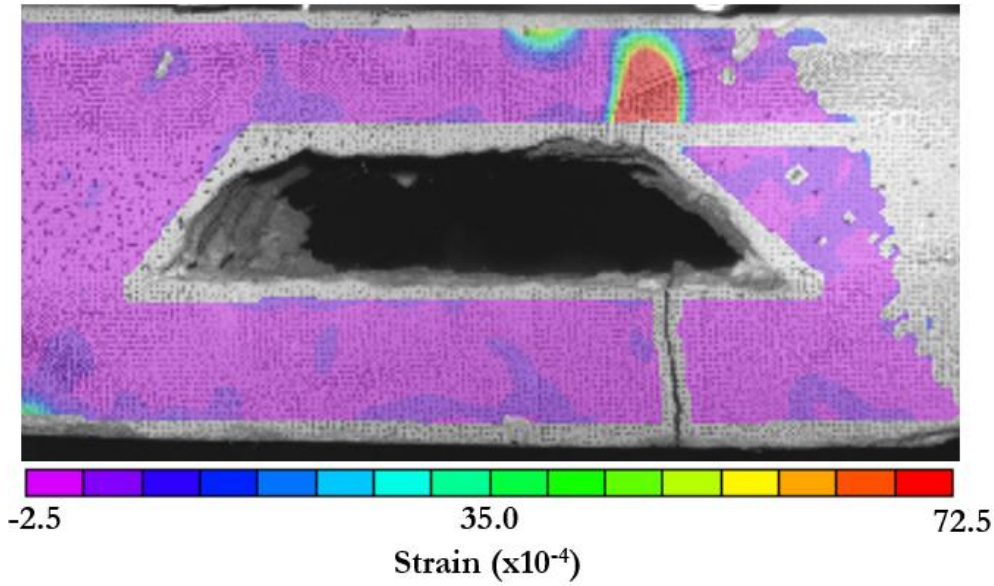

Figure 32. DIC of 2nd optimized fiber printed beam in 2nd generation after failure.

The behavior of the fiber beams can also be examined through the lens of the load-displacement curves. Figure 33 displays the load-displacement curve for the second optimized fiber beam. Unexpectedly, there is a large jump in post-peak behavior. A potential reason for the jump is the fact that the crack fully propagated due to the thin flange, causing the tension to be passed from the mortar to the fibers suddenly.

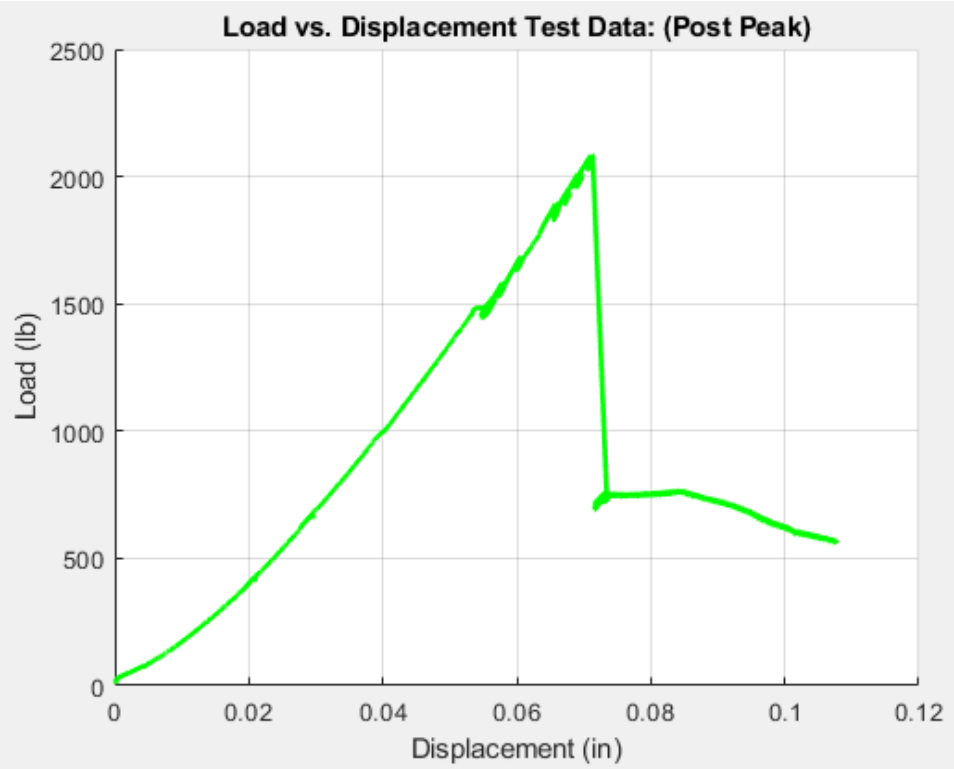

Figure 33. 2nd Generation fiber optimized print #2 load-displacement data.

Additional load-displacement data can be found in Appendix A. For the solid beams, the instantaneous jump to post-peak behavior is believed to be due to the displacement rate being too high.

CONCLUSIONS

The large-scale printing conducted in the project demonstrates key features of the 3D printing process. Firstly, large-scale printing must aim to have a continuous print path to avoid weak joints. If a continuous print path is not possible, pre-extrusion must be utilized to fill gaps and ensure bonding at the interface of paths. Secondly, care must be taken to prevent shrinkage cracking by keeping the print from drying and ensuring flowability over the duration of the print.

The results of the large-scale prints demonstrated that material usage of flexural elements can be heavily reduced by producing a generation of printed beams with comparable load carrying capacities to their solid counterparts. If proper interface bonding is ensured, the optimized beams will fail in the same mode as solid beams. If proper bonding is not maintained, optimized beams can fail in shear, but maintain comparable failure loads. Adding fibers to a mix enhances interface bonding and can prevent shear failure due to weak interface bonding.

Future explorations into topology optimization of 3D printed elements should attempt to better model flexural elements by extending the models beyond linear elastic and explore a wider array of load cases. Additional reinforced beams should also be printed to better capture the post-peak behavior of optimized beams.

REFERENCES

Asprone, D., Auricchio, F., Menna, C., & Mercuri, V. (2018). 3D printing of reinforced concrete elements: Technology and design approach. *Construction and Building Materials*, *165*, 218–231. https://doi.org/https://doi.org/10.1016/j.conbuildmat.2018.01.018

Borg Costanzi, C., Ahmed, Z. Y., Schipper, H. R., Bos, F. P., Knaack, U., & Wolfs, R. J. M. (2018). 3D Printing Concrete on temporary surfaces: The design and fabrication of a concrete shell structure. *Automation in Construction*, *94*, 395–404. https://doi.org/https://doi.org/10.1016/j.autcon.2018.06.013

Bos, F., Wolfs, R., Ahmed, Z., & Salet, T. (2016). Additive manufacturing of concrete in construction: potentials and challenges of 3D concrete printing. *Virtual and Physical Prototyping*, *11*(3), 209–225. https://doi.org/10.1080/17452759.2016.1209867

Chandra, P. S., van Zijl Gideon, P. A. G., Tan, M. J., & Gibson, I. (2018). A review of 3D concrete printing systems and materials properties: current status and future research prospects. *Rapid Prototyping Journal*, *24*(4), 784–798. http://login.ezproxy1.lib.asu.edu/login?url=https://search-proquest-com.ezproxy1.lib.asu.edu/docview/2058983421?accountid=4485

Chen, M., Yang, L., Zheng, Y., Huang, Y., Li, L., Zhao, P., Wang, S., Lu, L., & Cheng, X. (2020). Yield stress and thixotropy control of 3D-printed calcium sulfoaluminate cement composites with metakaolin related to structural build-up. *Construction and Building Materials*, *252*, 119090. https://doi.org/https://doi.org/10.1016/j.conbuildmat.2020.119090

De Schutter, G., Lesage, K., Mechtcherine, V., Nerella, V. N., Habert, G., & Agusti-Juan, I. (2018). Vision of 3D printing with concrete — Technical, economic and environmental potentials. *Cement and Concrete Research*, *112*, 25–36. https://doi.org/https://doi.org/10.1016/j.cemconres.2018.06.001

Hosseini, E., Zakertabrizi, M., Korayem, A. H., & Xu, G. (2019). A novel method to enhance the interlayer bonding of 3D printing concrete: An experimental and computational investigation. *Cement and Concrete Composites*, *99*, 112–119. https://doi.org/10.1016/j.cemconcomp.2019.03.008

Jeong, H., Han, S.-J., Choi, S.-H., Lee, Y. J., Yi, S. T., & Kim, K. S. (2019). Rheological Property Criteria for Buildable 3D Printing Concrete. *Materials*, *12*(4). https://doi.org/10.3390/ma12040657

Langelaar, M. (2016). Topology optimization of 3D self-supporting structures for additive manufacturing. *Additive Manufacturing*, *12*, 60–70. https://doi.org/https://doi.org/10.1016/j.addma.2016.06.010

Liu, J., Gaynor, A. T., Chen, S., Kang, Z., Suresh, K., Takezawa, A., Li, L., Kato, J., Tang, J., Wang, C. C. L., Cheng, L., Liang, X., & To, A. C. (2018). Current and future trends in topology optimization for additive manufacturing. *Structural and Multidisciplinary Optimization*, *57*(6), 2457–2483. https://doi.org/10.1007/s00158-018-1994-3

Longxuan, W., Wenfeng, D., Pengfei, H., & Mijia, Y. (2020). Topology Optimization and 3D Printing of Three-Branch Joints in Treelike Structures. *Journal of Structural Engineering*, *146*(1), 04019167. https://doi.org/10.1061/(ASCE)ST.1943-541X.0002454

Lowke, D., Dini, E., Perrot, A., Weger, D., Gehlen, C., & Dillenburger, B. (2018). Particle-bed 3D printing in concrete construction – Possibilities and challenges. *Cement and Concrete Research*, *112*, 50–65. https://doi.org/https://doi.org/10.1016/j.cemconres.2018.05.018

Marchment, T., & Sanjayan, J. (2020). Mesh reinforcing method for 3D Concrete Printing. *Automation in Construction*, *109*, 102992. https://doi.org/https://doi.org/10.1016/j.autcon.2019.102992

Mazhoud, B., Perrot, A., Picandet, V., Rangeard, D., & Courteille, E. (2019). Underwater 3D printing of cement-based mortar. *Construction and Building Materials*, *214*, 458–467. https://doi.org/https://doi.org/10.1016/j.conbuildmat.2019.04.134

Nana, A., Cuillière, J.-C., & Francois, V. (2017). Automatic reconstruction of beam structures from 3D topology optimization results. *Computers & Structures*, *189*, 62–82. https://doi.org/https://doi.org/10.1016/j.compstruc.2017.04.018

Panda, B., & Tan, M. J. (2018). Experimental study on mix proportion and fresh properties of fly ash based geopolymer for 3D concrete printing. *Ceramics International*, *44*(9), 10258–10265. https://doi.org/https://doi.org/10.1016/j.ceramint.2018.03.031

Panda, B., Tay, Y. W. D., Paul, S. C., & Tan, M. J. (2018). Current challenges and future potential of 3D concrete printing. *Materialwissenschaft Und Werkstofftechnik*, *49*(5), 666–673. https://doi.org/10.1002/mawe.201700279

Panda, B., Singh, G. V. P. B., Unluer, C., & Tan, M. J. (2019). Synthesis and characterization of one-part geopolymers for extrusion based 3D concrete printing. *Journal of Cleaner Production*, *220*, 610–619. https://doi.org/https://doi.org/10.1016/j.jclepro.2019.02.185

Podroužek, J., Marcon, M., Ninčević, K., & Wan-Wendner, R. (2019). Bio-Inspired 3D Infill Patterns for Additive Manufacturing and Structural Applications. *Materials*, *12*(3). https://doi.org/10.3390/ma12030499

Safonov, A. A. (2019). 3D topology optimization of continuous fiber-reinforced structures via natural evolution method. *Composite Structures*, *215*, 289–297. https://doi.org/https://doi.org/10.1016/j.compstruct.2019.02.063

Salet, T. A. M., Ahmed, Z. Y., Bos, F. P., & Laagland, H. L. M. (2018). Design of a 3D printed concrete bridge by testing. *Virtual and Physical Prototyping*, *13*(3), 222–236. https://doi.org/10.1080/17452759.2018.1476064

Tay, Y. W. D., Li, M. Y., & Tan, M. J. (2019). Effect of printing parameters in 3D concrete printing: Printing region and support structures. *Journal of Materials Processing Technology*, *271*, 261–270. https://doi.org/https://doi.org/10.1016/j.jmatprotec.2019.04.007

Vantyghem, G., De Corte, W., Shakour, E., & Amir, O. (2020). 3D printing of a post-tensioned concrete girder designed by topology optimization. *Automation in Construction*, *112*, 103084. https://doi.org/https://doi.org/10.1016/j.autcon.2020.103084

Xiong, Y., Yao, S., Zhao, Z. L., & Xie, Y. M. (2020). A new approach to eliminating enclosed voids in topology optimization for additive manufacturing. *Additive Manufacturing*. https://doi.org/10.1016/j.addma.2019.101006

Xu, Y., Zhang, H., Schlangen, E., Luković, M., & Šavija, B. (2020). Cementitious cellular composites with auxetic behavior. *Cement and Concrete Composites*, *111*, 103624. https://doi.org/https://doi.org/10.1016/j.cemconcomp.2020.103624

Zhang, Y., Zhang, Y., Liu, G., Yang, Y., Wu, M., & Pang, B. (2018). Fresh properties of a novel 3D printing concrete ink. *Construction and Building Materials*, *174*, 263–271. https://doi.org/https://doi.org/10.1016/j.conbuildmat.2018.04.115

APPENDIX A

FOUR POINT BENDING TEST DATA

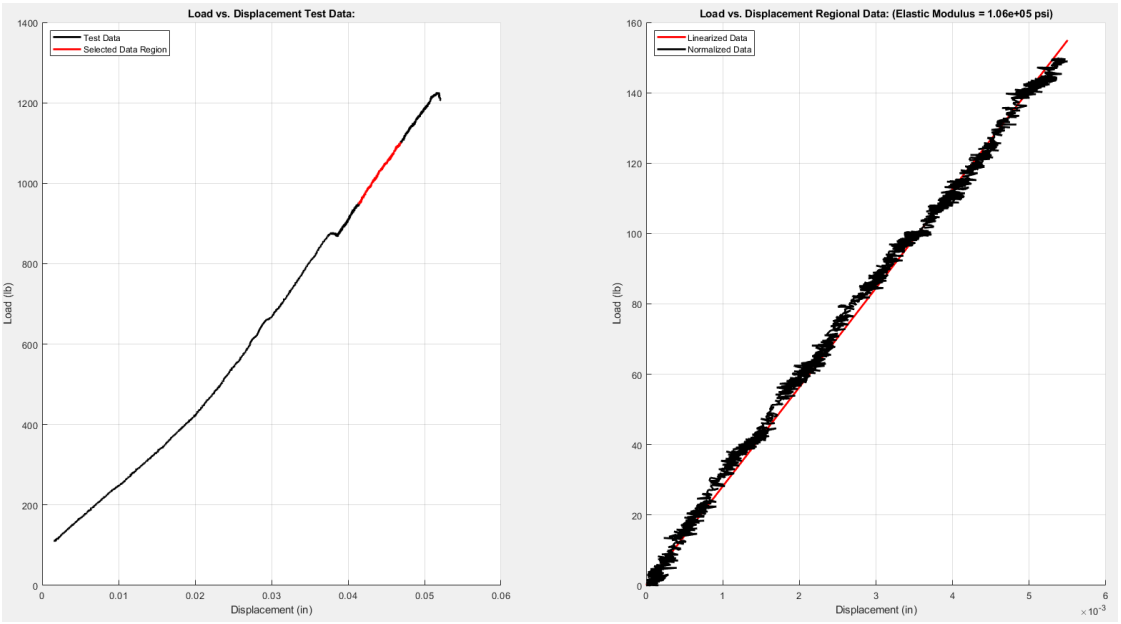

Figure 34. 2nd Generation cast #1 load-displacement data and region used for calculating young's modulus.

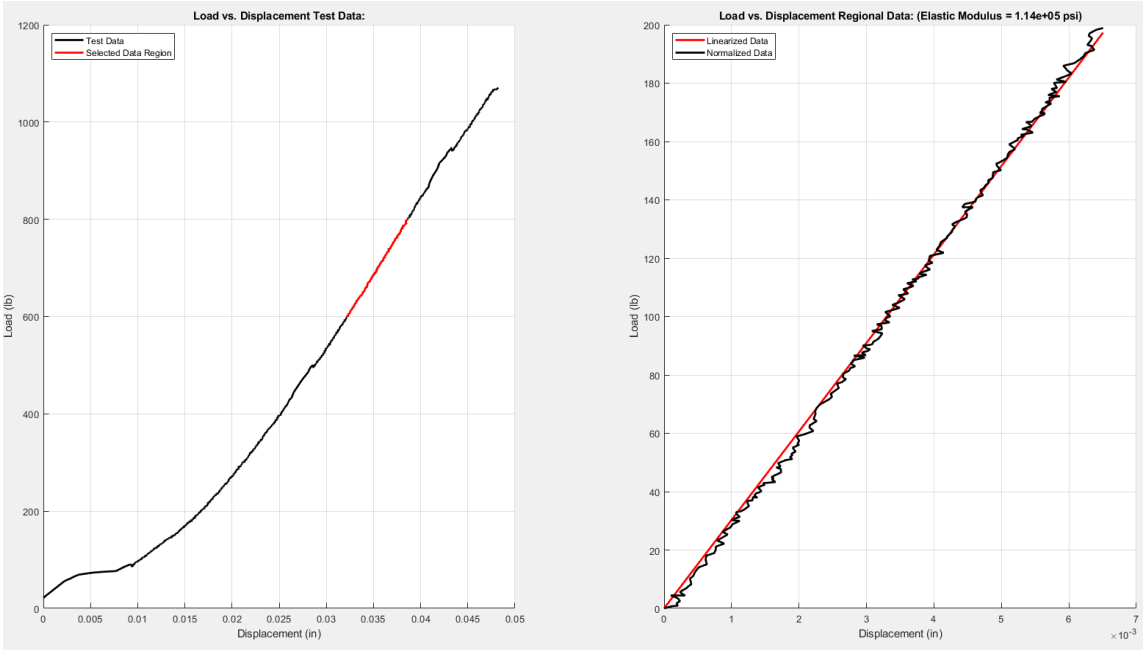

Figure 35. 2nd Generation cast #2 load-displacement data and region used for calculating young's modulus.

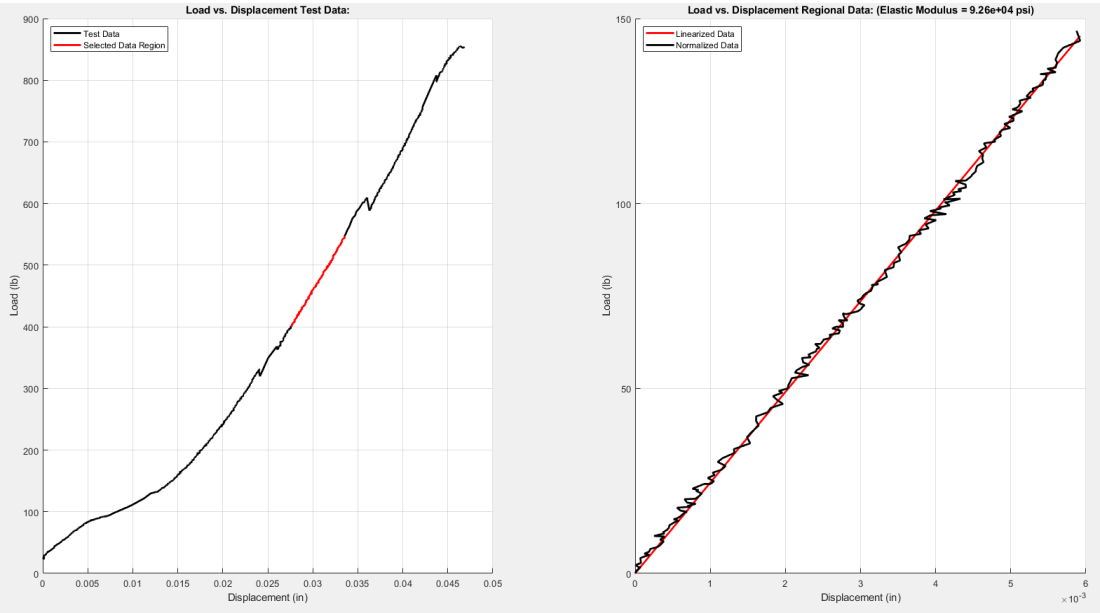

Figure 36. 2nd Generation cast #3 load-displacement data and region used for calculating young's modulus.

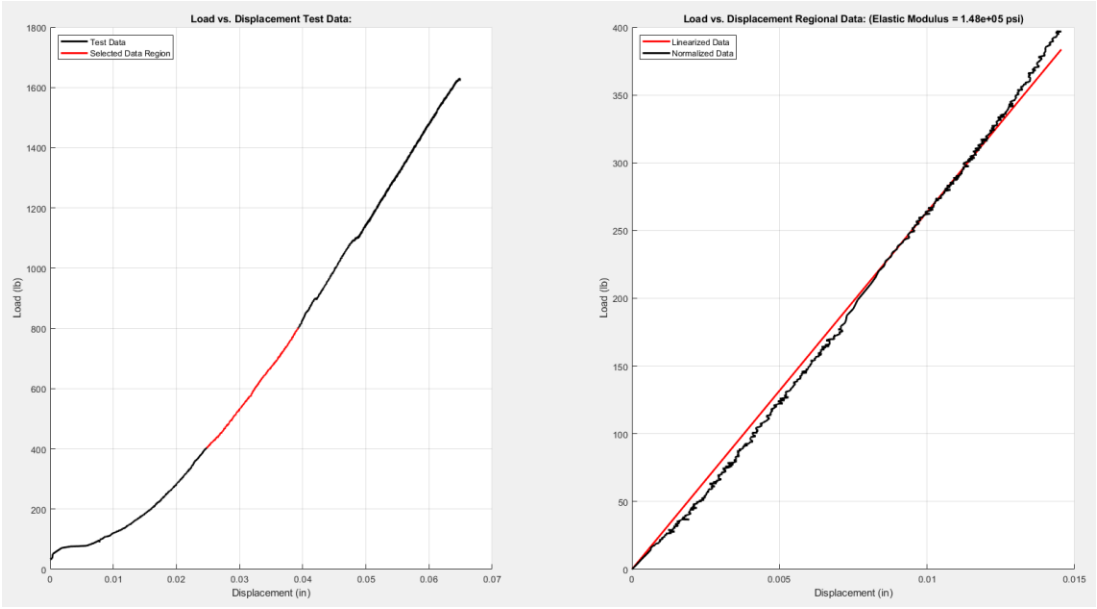

Figure 37. 2nd Generation solid print load-displacement data and region used for calculating young's modulus.

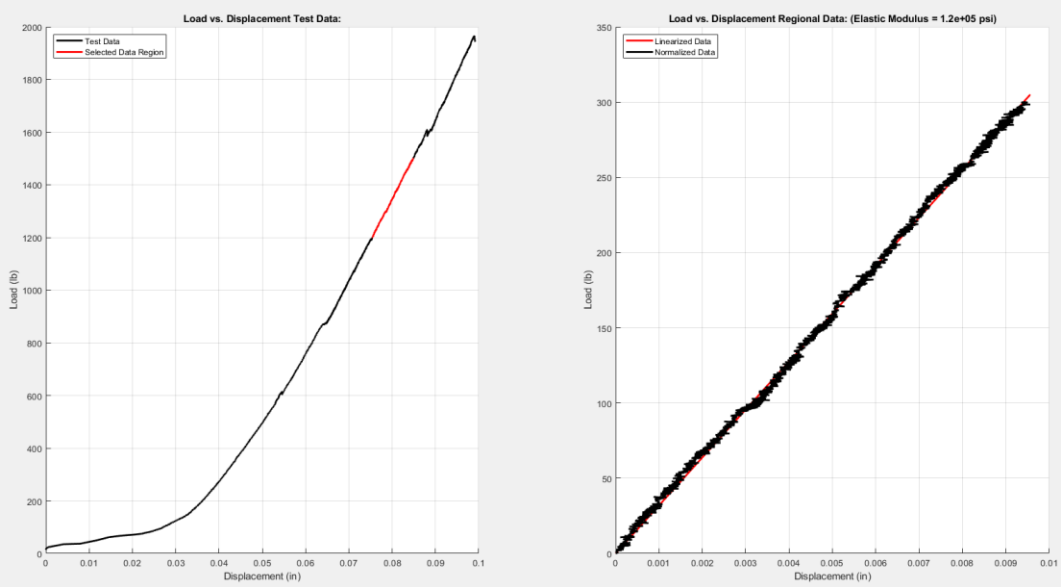

Figure 38. 2nd Generation optimized print #1 load-displacement data and region used for calculating young's modulus.

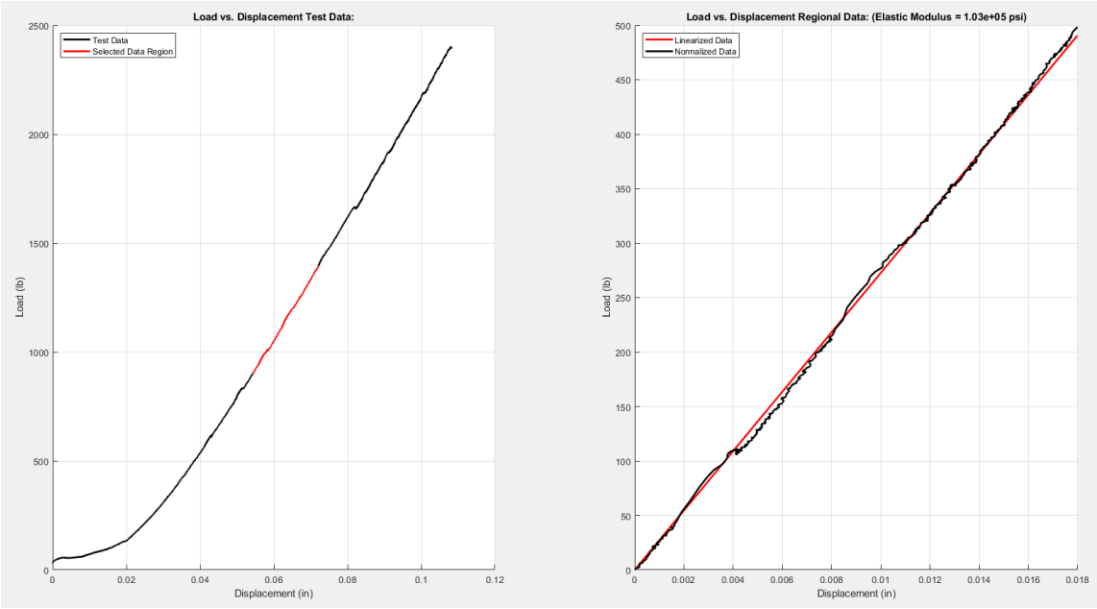

Figure 39. 2nd Generation optimized print #2 load-displacement data and region used for calculating young's modulus.

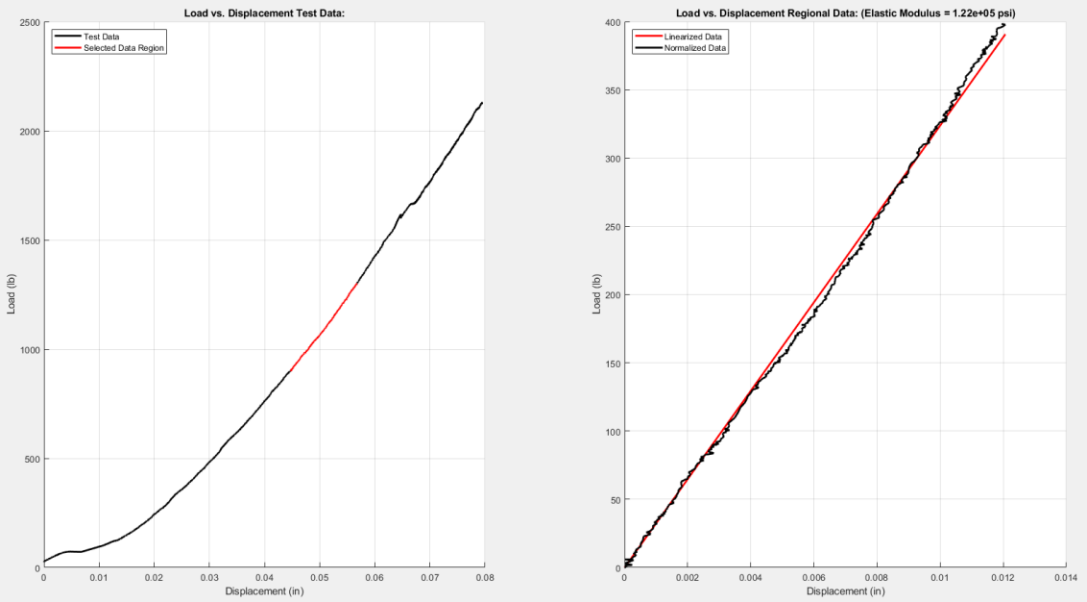

Figure 40. 2nd Generation optimized print #3 load-displacement data and region used for calculating young's modulus.

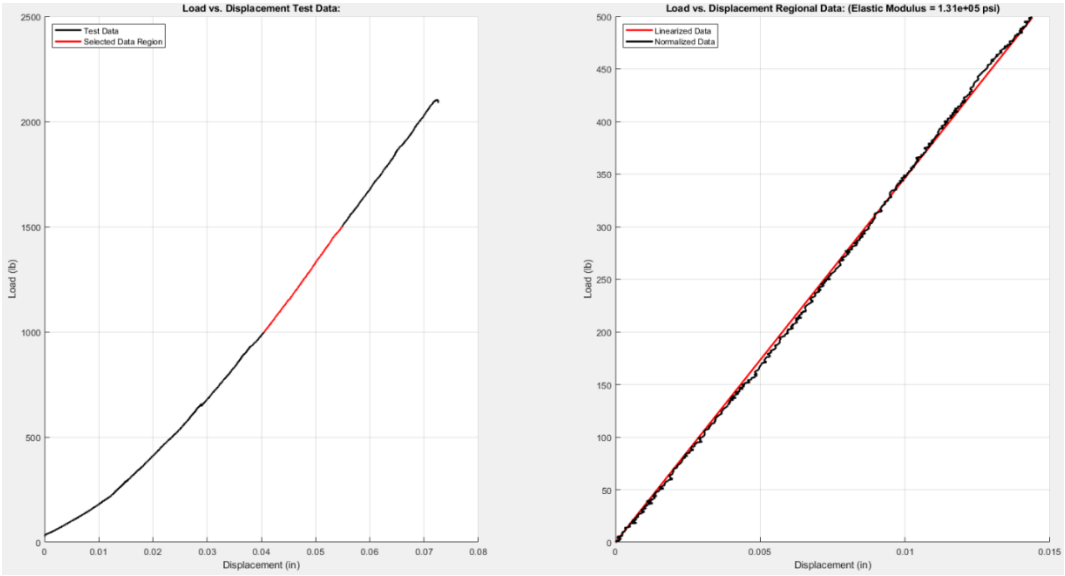

Figure 41. 2nd Generation optimized print #4 load-displacement data and region used for calculating young's modulus.

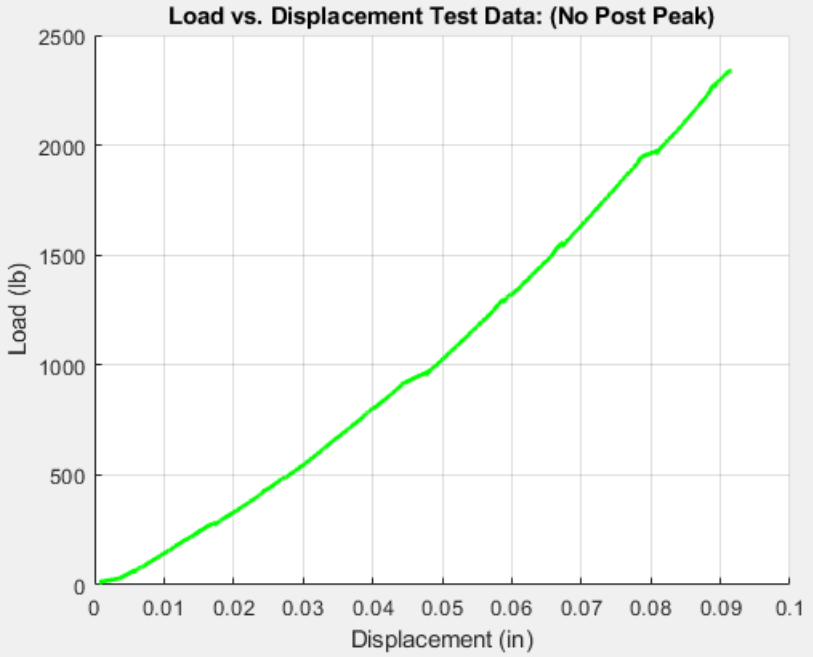

Figure 42. 2nd Generation fiber cast #1 load-displacement data.

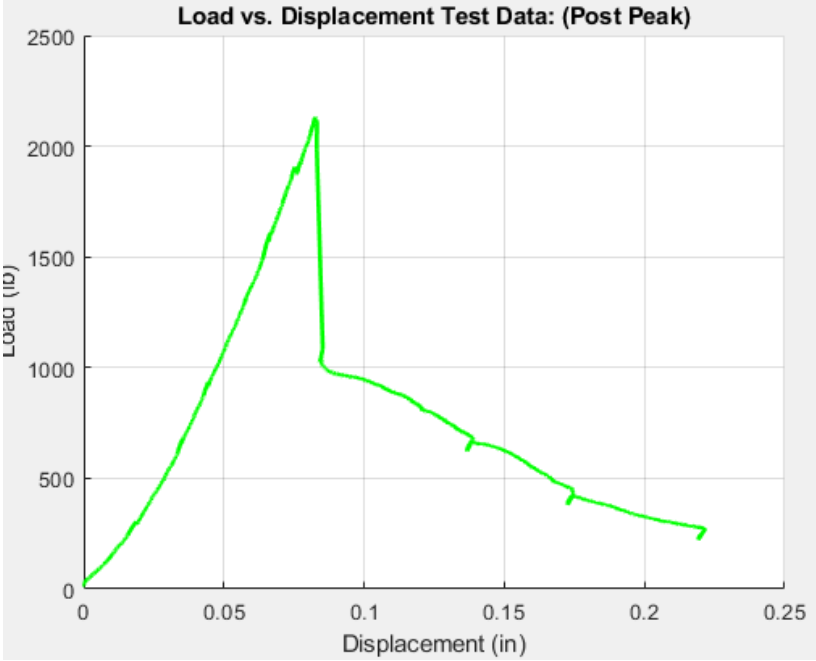

Figure 43. 2nd Generation fiber cast #2 load-displacement data.

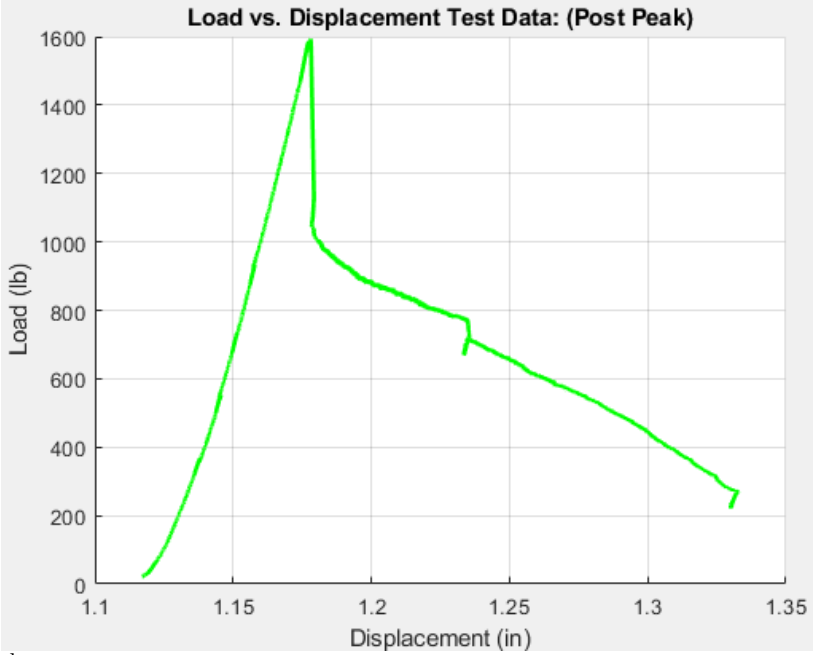

Figure 44. 2nd Generation fiber solid print #1 load-displacement data.

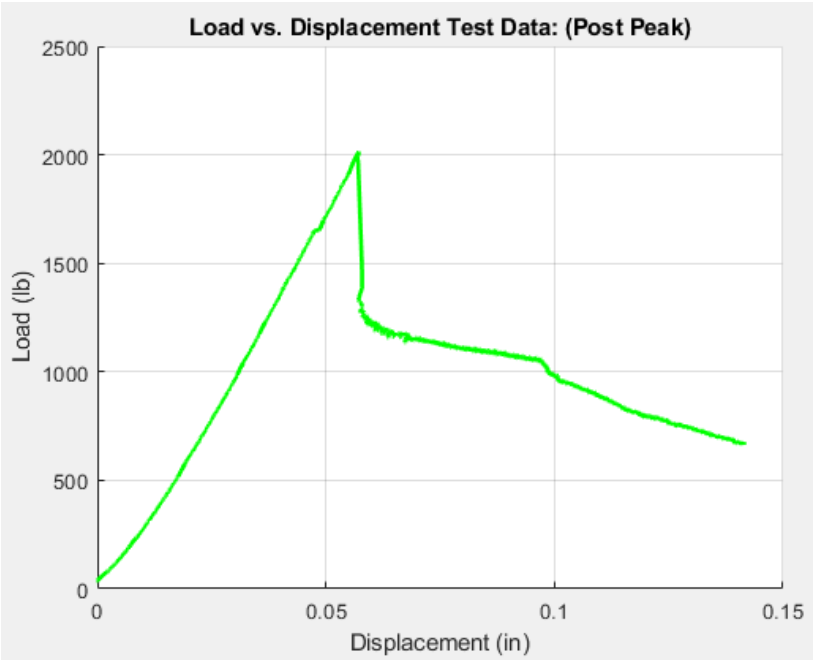

Figure 45. 2nd Generation fiber solid print #2 load-displacement data.

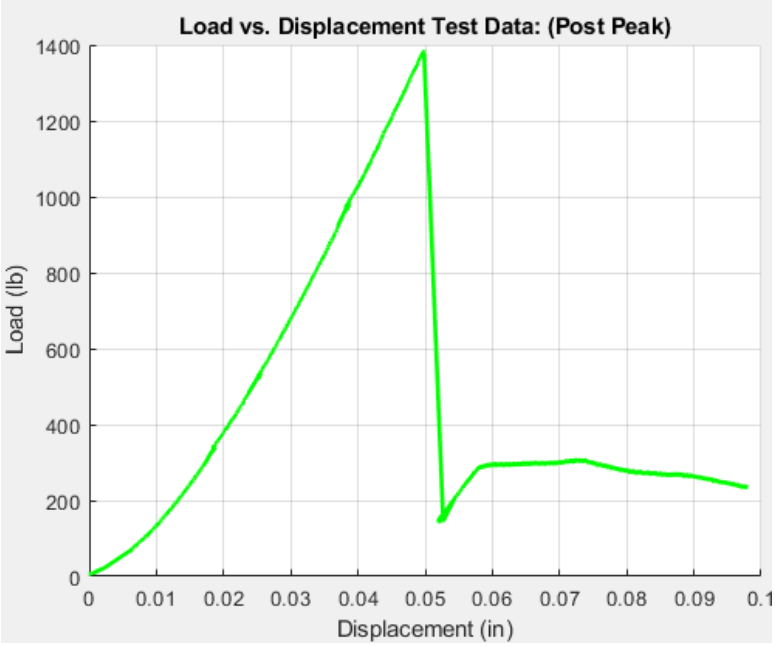

Figure 46. 2nd Generation fiber optimized print #1 load-displacement data.

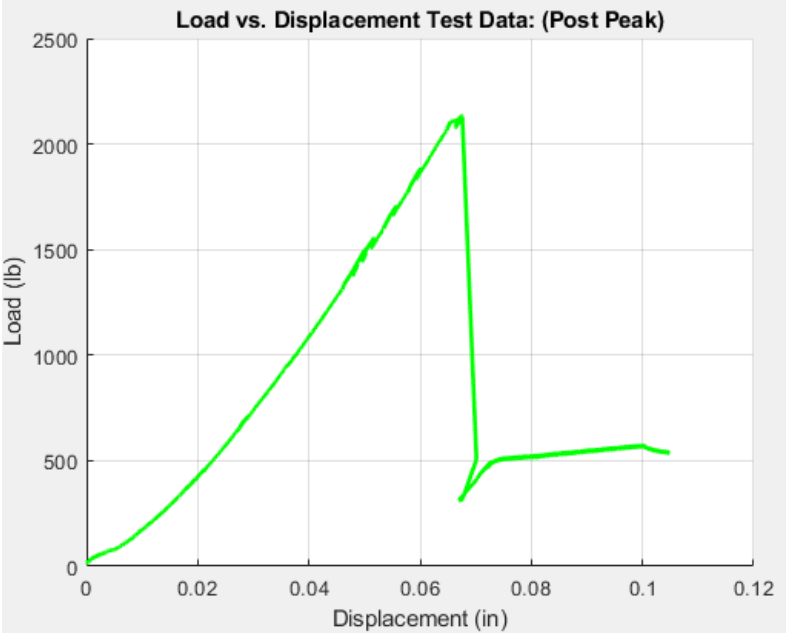

Figure 47. 2nd Generation fiber optimized print #2 load-displacement data.